Growth and geometry split in light of the DES-Y3 survey

Kunhao Zhong,[1,*] Evan Saraivanov,[1] Vivian Miranda,[1,2] Jiachuan Xu,[3] Tim Eifler,[3] and Elisabeth Krause[3,4]

[1]*Department of Physics and Astronomy, Stony Brook University, Stony Brook, New York 11794, USA*
[2]*C. N. Yang Institute for Theoretical Physics, Stony Brook University, Stony Brook, New York, 11794, USA*
[3]*Department of Astronomy/Steward Observatory, University of Arizona, 933 North Cherry Avenue, Tucson, Arizona 85721, USA*
[4]*Department of Physics, University of Arizona, 1118 E Fourth Street, Tucson, Arizona, 85721-0065, USA*

(Received 18 January 2023; accepted 5 June 2023; published 21 June 2023)

We test the smooth dark energy paradigm using Dark Energy Survey (DES) year 1 and year 3 weak lensing and galaxy clustering data. Within the ΛCDM and *w*CDM model we separate the expansion and structure growth history by splitting Ω_m (and w) into two metaparameters that allow for different evolution of growth and geometry in the Universe. We consider three different combinations of priors on geometry from CMB, SNIa, BAO, BBN that differ in constraining power but have been designed such that the growth information comes solely from the DES weak lensing and galaxy clustering. For the DES-Y1 data we find no detectable tension between growth and geometry metaparameters in both the ΛCDM and *w*CDM parameter space. This statement also holds for DES-Y3 cosmic shear and 3×2 pt analyses. For the combination of DES-Y3 galaxy-galaxy lensing and galaxy clustering (2×2 pt) we measure a tension between our growth and geometry metaparameters of 2.6σ in the ΛCDM and 4.48σ in the *w*CDM model space, respectively. We attribute this tension to residual systematics in the DES-Y3 RedMaGiC galaxy sample rather than to new physics. We plan to investigate our findings further using alternative lens samples in DES-Y3 and future weak lensing and galaxy clustering datasets.

DOI: 10.1103/PhysRevD.107.123529

I. INTRODUCTION

Since the discovery of the accelerated expansion of our Universe [1,2], the flat ΛCDM, which adopts a late-time Universe dominated by the cosmological constant, has become the standard model of cosmology. From a fundamental physics viewpoint, the origin of dark energy is still unknown. The cosmological constant modeled as vacuum energy is fine-tuned with a value too small to any known quantum field theory [3]. Dynamical scalar fields, *quintessence* and *k-essence*, have been proposed to solve the fine-tuning problem [4–8]. Modified gravity is an alternative way to explain the Universe's acceleration without introducing a new component [9]. To date, none of these proposed scenarios have been detected by observations.

With only six free parameters, the standard model of cosmology predicts the temperature and polarization anisotropy statistics of the cosmic microwave background (CMB) with remarkable success. Additionally, imaging and spectroscopic surveys show increasing power to constrain ΛCDM's predictions for the late-time evolution of large-scale structures (LSS); current stage III LSS surveys include the Dark Energy Survey (DES) [10–18], the Kilo-Degree Survey (KiDS) [19–23], the Hyper Suprime-Cam Subaru Strategic Program (HSC) [24–28], and the Baryon Oscillation Spectroscopic Survey (Boss and eBOSS) [29–34].

However, multiple tensions have arisen in the last few years within the ΛCDM model, particularly between Planck measurements of the cosmic microwave background and data from the late-time Universe. The first tension involves the value of the Hubble constant, H_0 [35–38]. Local-Universe H_0 estimates from type Ia supernova (SNIa), calibrated using Cepheid variable stars [39,40], conflict with CMB predictions [41,42]. Several studies show that this tension is reaching a statistical significance of 5σ [36–38].

Hubble constant predictions from the cosmic microwave background are sensitive to changes in the late-time dark sector [43]. For example, cold dark matter models decaying to relativistic species can affect the CMB predictions [44–46]. These predictions are also sensitive to physics before recombination via the sound horizon. However, observations of SNIa combined with baryonic acoustic oscillations (BAO) show that changes in the late-time Universe dark sector cannot solve the H_0 tension without creating additional problems [47–49]. These constraints suggest that the new physics should come from the time before recombination [50,51].

The Dark Energy Survey year one (DES-Y1) and year three (DES-Y3) analysis conclude that the parameter S_8 is in mild tension with the ΛCDM model predicted by Planck CMB data [52–54]. Multiple independent surveys have independently discovered this discrepancy [20,31,55,56].

*kunhao.zhong@stonybrook.edu

The projected one-dimensional S_8 tension is not large; however, investigations of the multidimensional degeneracy directions in ΛCDM parameter space offers a more complete picture [57]. The generalizations of the late-time dark sector can reduce this discrepancy, but the S_8 tension generally increases with statistical significance when an early-dark energy component is added in the ΛCDM model [58–60].

In this work, we split the matter density, Ω_m, and the dark energy equation of state, w, to test the consistency of smooth-dark-energy between the background evolution and the late-time scale-independent growth of structures [61–65]. Using different datasets containing geometry or growth information, we can verify such consistency in ΛCDM and wCDM models. Parameter splitting has been extensively applied in multiple contexts. For example, baryon density can be divided into two parts with one only affecting ionization history [66], cold matter density can be split into parts representing different aspects of type Ia supernova [67], or the primordial inflationary amplitude can be separated into one that affects the CMB and another that only affects predictions from the effective field theory of large-scale structure [68].

This work is a follow-up investigation of two previous analyses, one employing DES-Y1 data [69], and the other adopting older weak lensing data from the Canada-France Hawaii Telescope Lensing Survey [64]. In this work, we employ the new DES-Y3 3×2 pt data, including different data combinations that clarify some internal aspects of the galaxy-galaxy lensing and galaxy clustering combination. The Kilo-Degree Survey (KiDS) Collaboration also analyzed their data with the growth-geometry split type of parameters [23]. In addition to weak lensing and galaxy clustering, redshift space distortion (RSD) and clusters data are used to extract growth information [70,71]. Previous weak lensing work with DES-Y1 data [69] does not report a disagreement with the ΛCDM model. However, RSD data do favor a lower growth rate. See Sec. VI for a detailed discussion.

The structure of the paper is as follows: In Sec. II, we explain the geometry-growth split and the 3×2 pt combination of two-point correlation functions. We summarize DES analysis choices and the external datasets in Sec. IV, which also contains a detailed description of our adopted pipeline and the validation tests we performed based on synthetic ΛCDM DES-Y1 and DES-Y3 data vectors. We present the results and discussions in Sec. V, and conclusions, including an exposition on planned follow-up improvements, in Sec. VI.

II. THEORY AND METHODOLOGY

A. Split matter power spectrum

The linear matter power spectrum quantifies the inhomogeneity of matter distribution, and it can be written as the product of the inflationary primordial spectrum, the transfer function, and the growth function,

$$P^{\rm linear}(z,k)=\frac{2\pi^2}{k^3}\frac{4}{25}A_s\left(\frac{k}{k_{\rm norm}}\right)^{n_s-1}\left(\frac{k}{H_0}\right)^4\times T^2(k)\left(\frac{G(z)}{\Omega_m(1+z)}\right)^2. \quad (1)$$

The growth function,

$$G(z)=(1+z)D(z)=(1+z)\frac{\delta_m(z)}{\delta_m(z_{\rm ini})}, \quad (2)$$

describes the scale-independent time evolution of matter overdensity from initial conditions defined at redshift $z_{\rm ini}=1000$. In smooth dark energy cosmologies, the growth-factor evolution obeys the following ordinary differential equation:

$$G''+\left(4+\frac{H'}{H}\right)G'+\left[3+\frac{H'}{H}-\frac{3}{2}\Omega_m(z)\right]G=0, \quad (3)$$

where the prime denotes derivative with respect to the logarithm of the scale factor, $\ln a$. The initial conditions are $G_{\rm ini}=1$ and $G'_{\rm ini}=-(3/5)(1-w)\Omega_{\rm DE}(z_{\rm ini})$ [62]. Models that introduce clustering of dark energy break this scale-independent relation between growth factor and dark energy parameters [72,73]. In this work, we confine our study to the case of smooth dark energy with a constant equation of state (wCDM). Our results can be generalized, for example, by considering instead principal component based $w(z)$ parametrizations [65,74].

We split the Ω_m and w parameters into geometry, $\{\Omega_m^{\rm geo},w^{\rm geo}\}$, and growth counterparts $\{\Omega_m^{\rm growth},w^{\rm growth}\}$. The growth parameters affect the late-time growth factor evolution via Eq. (3). The remaining parameters, $\{\Omega_b,H_0,A_s,n_s,\tau\}$, are not split. The split ΛCDM cosmology assumes $w^{\rm geo}=w^{\rm growth}=-1$. Since the linear power spectrum $P^{\rm linear}(z,k)\propto G^2(z)$, we can define the split linear matter power spectrum to be

$$P^{\rm linear}_{\rm split}(k,z)=\frac{P^{\rm linear-camb}_{\rm geo}(k,z)}{G^{\rm camb}_{\rm geo}(z)^2}\times G_{\rm growth}(z)^2, \quad (4)$$

with

$$G_{\rm growth}(z)=G^{\rm camb}_{\rm geo}(z)\times\left(\frac{G^{\rm ODE}_{\rm growth}(z)}{G^{\rm ODE}_{\rm geo}(z)}\right). \quad (5)$$

$P^{\rm linear-camb}_{\rm geo}$ and $G^{\rm camb}_{\rm geo}$ are respectively the linear power spectrum and the growth factor both computed by the Boltzmann code CAMB [75,76] assuming the geometry parameters. $G^{\rm ODE}_{\rm geo}$ and $G^{\rm ODE}_{\rm growth}$ are solutions of the differential Eq. (3) given geometry and growth parameters respectively.

Our slightly convoluted definition is analytically equivalent to

$$P^{\rm linear}_{\rm split}(k,z)=P^{\rm linear-camb}_{\rm geo}(k,z)\times\left(\frac{G^{\rm ODE}_{\rm growth}(z)}{G^{\rm ODE}_{\rm geo}(z)}\right)^2. \quad (6)$$

Definition of Eq. (5) resolves the small numerical error between the growth factor calculated by CAMB versus the solution from Eq. (3) with no radiation and accurate background evolution of massive neutrinos; the adopted multiprobe lensing pipeline requires $G_{\rm growth}(z)$ itself when computing intrinsic alignment contributions for cosmic shear and galaxy-galaxy lensing.

We follow the naming convention in the parameter split literature. In our parameter split distance probes heavily constrain geometry parameters while growth parameters allow the late-time growth factor to vary with extra degrees of freedom. However $\Omega_{\rm m}^{\rm geo}$ and $w^{\rm geo}$ can also affect structure growth. Specifically, the split matter power spectrum in our definition is proportional to $(\Omega_{\rm m}^{\rm geo})^{-2}$ (see Fig. 1). Additionally, early universe physics that affect both background expansion and structure formation are also modeled by $\Omega_{\rm m}^{\rm geo}$. The split between geometry and growth is not uniquely defined, and we defer to future work examining the impact of these choices. The root mean variance within 8 Mpc/h is defined as

$$\sigma_8^2(z) = \frac{1}{2\pi^2}\int {\rm d}\log k W^2(kR)k^3P(k,z), \tag{7}$$

where $W(kR)$ is a top-hat filter function in Fourier space with radius $R = 8$ Mpc/h. The split $\sigma_8^{\rm split}(z)$ is then given by

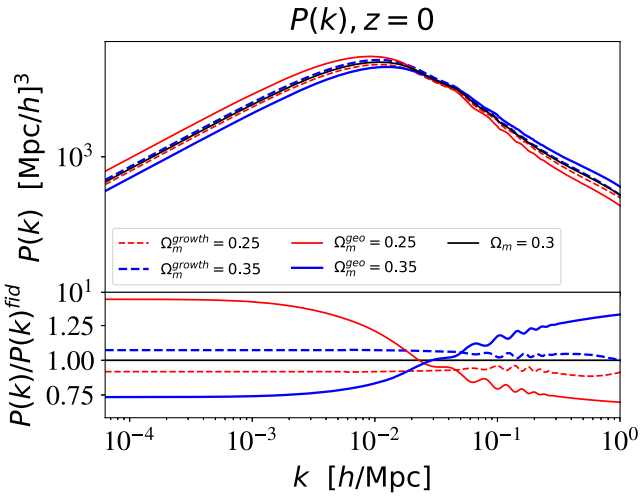

FIG. 1. Geometry and growth effects on the matter power spectrum in the split-ΛCDM model. When changing one parameter, we keep the remaining matter density at $\Omega_{\rm m}^{\rm X} = 0.3$. The choice of employing $\Omega_{\rm m}^{\rm growth}$ in the Euclid Emulator has the effect of roughly maintaining the scale-independent amplitude shift induced by changes in $\Omega_{\rm m}^{\rm growth}$ on mildly nonlinear scales. On $k \gtrsim 10^{-2}$ scales that are within DES reach, changes in the shape parameter $\Gamma = \Omega_{\rm m}^{\rm geo}h$ induced by varying $\Omega_{\rm m}^{\rm geo}$ are degenerate with the primordial power spectrum tilt, $n_{\rm s}$. This degeneracy motivates our choice of priors; CMB brings external constraints on the inflationary and shape parameters, while BAO and SNIa indirectly limits the shape parameter.

$$\sigma_8^{\rm split}(z) = \sigma_8^{\rm geo-camb}(z) \times \left(\frac{G_{\rm growth}^{\rm ODE}(z)}{G_{\rm geo}^{\rm ODE}(z)}\right). \tag{8}$$

The different behavior of $\sigma_8^{\rm split}(z)$ versus $\sigma_8(z)$ with respect to the change of growth and geometry parameters is shown in Fig. 2. In the split ΛCDM case, the change of $\Omega_{\rm m}^{\rm growth}$ will give a smaller change on $\sigma_8(z)$ compared with the nonsplit case, namely when changing $\Omega_{\rm m}^{\rm growth}$ and $\Omega_{\rm m}^{\rm geo}$ simultaneously. In the split wCDM case a change in $w^{\rm growth}$ gives the same change as in the nonsplit case. In both cases, the change is larger at low redshift.

To account for nonlinearities in the split power spectrum, we utilize the Euclid Emulator to compute the factor $B(k,z) \equiv P(k,z)/P^{\rm linear}(k,z)$ [77]. In this work, we defined the

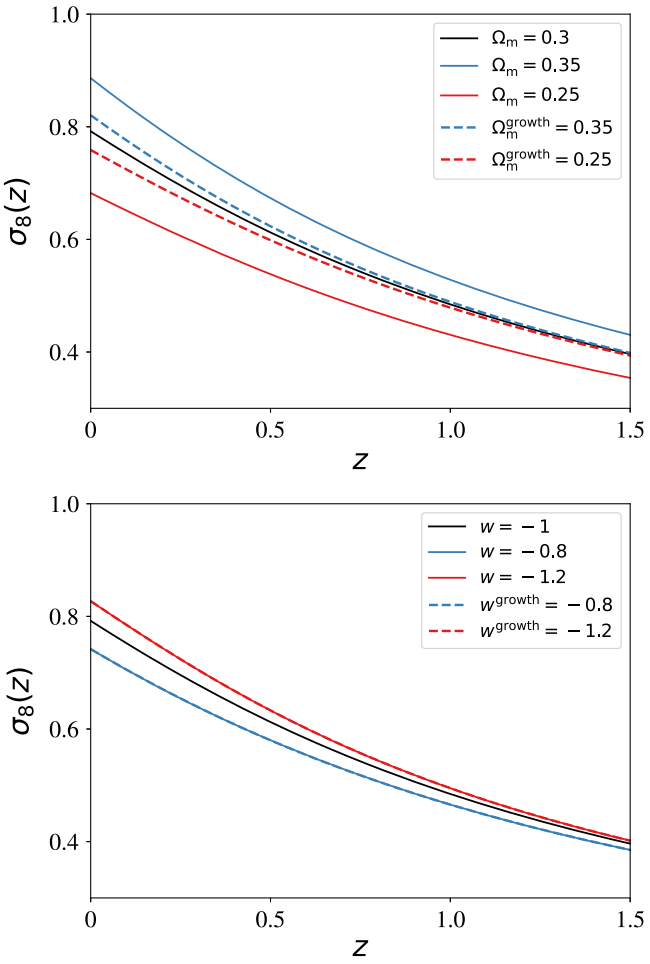

FIG. 2. Both panels show σ_8 changes under the variations of the unsplit and split $\Omega_{\rm m}$ and w parameters. The solid lines show shifts on the unsplit ΛCDM and wCDM models, and the dashed lines change growth while keeping the geometry parameters at their fiducial $\Omega_{\rm m}^{\rm geo} = 0.3$ and $w^{\rm geo} = -1$. We can see that changes in the growth parameter $\Omega_{\rm m}^{\rm growth}$ result in a minor shift in $\sigma_8(z)$, whereas $w^{\rm growth}$ gives the same change as in the nonsplit case because it only affects the matter power spectrum through the growth function.

$B(k,z)$ as dependent on the growth parameters. We then define the split matter power spectrum as

$$P_{\rm split}(k,z) = P^{\rm linear}_{\rm split}(k,z) \times B^{\rm growth}(k,z). \tag{9}$$

The official DES-Y1 and DES-Y3 analyses adopt Halofit. Figure 3 shows that Halofit and Euclid Emulator differences are within 5%. This disagreement does not affect inferences on the ΛCDM parameters as shown in the bottom panel of Fig. 3. However, our definition has practical advantages.

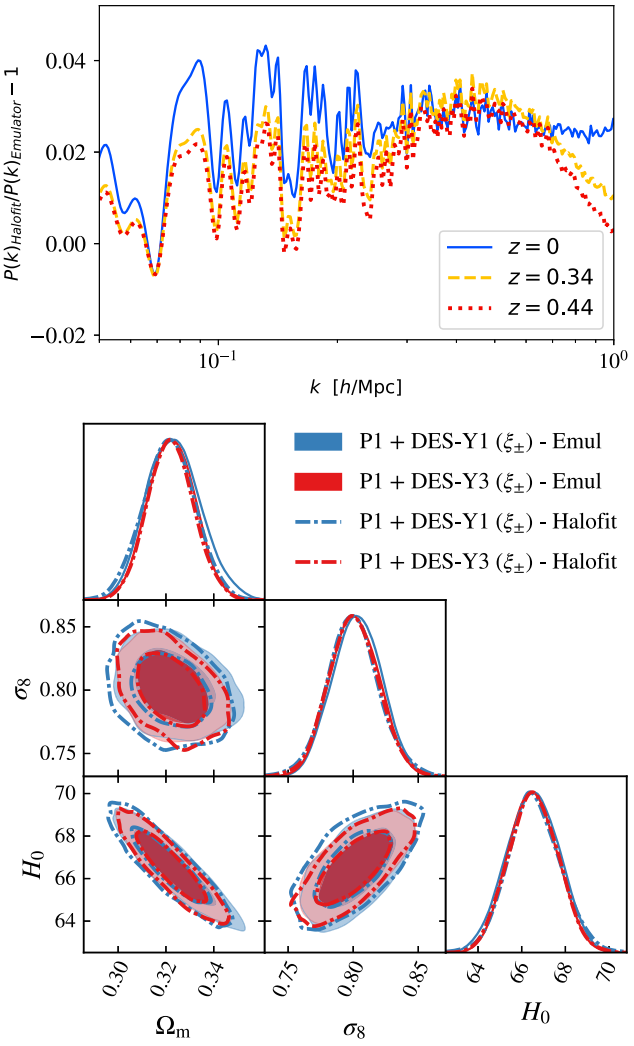

FIG. 3. Top panel: fractional difference of nonlinear power spectrum between Halofit and the Euclid Emulator at three different redshifts; Fiducial parameter values are the same adopted in the synthetic DES chains (see Sec. IV D). Bottom panel: posterior comparison between Halofit and the Euclid Emulator on P1 + DES-Y1/Y3 cosmic shear combinations (P1 prior is defined in Sec. IV B). We assumed the ΛCDM model in all four chains, and the DES-Y1/Y3 data vector was synthetic with the same fiducial model adopted in Sec. IV D. Both figures illustrate that within the prior ranges adopted in this manuscript, the few percent differences between Halofit and the Euclid Emulator do not impact our results.

Massive neutrinos break the scale-independent evolution of dark matter perturbations; neutrinos transition from relativistic to nonrelativistic behavior as the universe cools down. The scale-dependant changes in the matter spectrum are absorbed in $P^{\rm linear}_{\rm geo}(k,z)$ calculated by the Boltzmann code. For this paper, we only study fixed neutrino mass with $\sum_\nu m_\nu = 0.06$ eV.

III. TWO-POINT CORRELATION FUNCTIONS

A. Weak lensing and galaxy clustering

The dark matter distribution of the Universe is traced by two fields: (i) the galaxy density field and (ii) the weak lensing shear field. These fields generate three two-point correlation functions (2PCF) as a function of angular separation θ:

Cosmic shear $\xi^{ij}_\pm(\theta)$: the correlation, $\langle\kappa\kappa\rangle$, between source galaxy shear in redshift bins i and j.

Galaxy-galaxy lensing $\gamma^{ij}(\theta)$: the correlation, $\langle\delta_g\kappa\rangle$, between lens galaxy positions and source galaxy tangential shear in redshift bins i and j.

Galaxy clustering $w^{ij}(\theta)$: the correlation, $\langle\delta_g\delta_g\rangle$, between lens galaxy position in redshift bins i and j.

In combination, these probes significantly increase the information about the matter distribution and improve the systematics mitigation. Throughout this paper, "3 × 2 pt" refers to the multiprobe analysis involving the combination of the three 2PCF, and "2 × 2 pt" refers to the multiprobe combination of galaxy-galaxy lensing and galaxy clustering ($\gamma_t + w_\theta$).

Theory predictions and 2PCF are related by the angular power spectra. In both DES-Y1 and DES-Y3, we calculate the full non-Limber integral on large angles only in the galaxy position auto power spectra, following Fang *et al.* [78]. Using Limber approximation, the angular power spectra of tracer A at redshift bin i and tracer B at redshift bin j is [79,80]

$$C^{ij}_{AB}(\ell) = \int d\chi \frac{W^i_A(\chi) W^j_B(\chi)}{\chi^2(z)} P_{\rm split}(k, z(\chi))|_{k=(l+1/2)/\chi}, \tag{10}$$

where χ is the comoving radial distance. The weighting function of weak lensing shear κ and galaxy number density δ_g are respectively [81],

$$W^i_\kappa(\chi) = \frac{3H_0^2\Omega_{\rm m}^{\rm geo}}{2c^2}\frac{\chi}{a(\chi)}\int_\chi^\infty {\rm d}\chi' \frac{n^i_\kappa(z(\chi'))dz/d\chi'}{\bar{n}^i_\kappa}\frac{\chi'-\chi}{\chi'} \tag{11}$$

and

$$W^i_{\delta_g}(\chi) = b^i(z(\chi))\frac{n^i_{\rm g}(z(\chi))}{\bar{n}^i_{\rm g}}\frac{dz}{d\chi}. \tag{12}$$

Here, $\bar{n}^i_{g/\kappa} = \int dz n^i_{g/\kappa}(z)$ is the angular number density of galaxies in the redshift bin i, and $b^i(z(\chi))$ is the galaxy bias. Geometry parameters model the comoving radial distance [69]. Being consistent with Eq. (1), $P(k) \propto (1/\Omega_m^{geo})^2$, the matter density that appears in the W_κ prefactor is Ω_m^{geo}. This choice mainly follows the preferences of [69]. We defer the interesting investigation of how changing $\Omega_m^{geo} \to \Omega_m^{growth}$ here would affect the comparison between growth and geometry parameters.

The relation between two-point correlation functions and angular power spectra assumes bin-average curved sky formulas in both DES-Y1 and DES-Y3 as shown below,

$$w^i_\theta(\bar{\theta}) = \sum_\ell \frac{2\ell+1}{4\pi} \overline{P_\ell} C^{ii}_{\delta\delta}(\ell), \tag{13}$$

$$\begin{aligned}\gamma^{ij}_t(\bar{\theta}) &= \sum_\ell \frac{2\ell+1}{4\pi\ell(\ell+1)} \overline{P^2_\ell} C^{ij}_{\delta E}(\ell), \\ \xi^{ij}_\pm(\bar{\theta}) &= \sum_\ell \frac{2\ell+1}{2\pi\ell^2(\ell+1)^2} \overline{[G^+_{\ell,2} \pm G^-_{\ell,2}]} [C^{ij}_{EE}(\ell) \pm C^{ij}_{BB}(\ell)].\end{aligned} \tag{14}$$

The analytical expressions for Legendre and associated Legendre polynomials $\overline{P_\ell}$ and $\overline{G^\pm_{\ell,2}}$ can be found in [82]. Further information about these transformations, including E/B-mode projections on the auto and cross power spectra involving shear, are described in the DES-Y3 methods paper [16]. The computation of non-Limber integrals in galaxy position auto power spectra, and the use of bin-average curved sky formulas for cosmic shear, galaxy-galaxy lensing and galaxy clustering in DES-Y1 is an improvement over modeling choices of [69].

We use the tidal alignment and tidal torquing (TATT), a generalization to the previously DES-Y1 adopted nonlinear alignment model (NLA-IA), to model the intrinsic alignment of galaxies in DES-Y3 data [16,83,84]. Under this framework, the intrinsic shape of galaxies is written as a collection of terms depending on the matter overdensity, δ_m, and the tidal tensor, s_{ij}. These terms describe tidal alignment, tidal torquing, and density weighting, as shown below,

$$\gamma^I_{ij} = \underbrace{C_1 s_{ij}}_{\text{Tidal Alignment}} + \underbrace{b_{\rm TA} C_1 (\delta_m \times s_{ij})}_{\text{Density Weighting}} + \underbrace{C_2 \left[s^k_i s_{kj} - \frac{1}{3}\delta_{ij} s^2 \right]}_{\text{Tidal Torquing}}. \tag{15}$$

Here,

$$C_1 = -\frac{A_1 \bar{C} \Omega_m^{growth}}{a G^{growth}(z)} \left(\frac{1+z}{1+z_0} \right)^{\eta_1}, \tag{16}$$

and

$$C_2 = 5 \frac{A_2 \bar{C} \Omega_m^{growth}}{(a G^{growth}(z))^2} \left(\frac{1+z}{1+z_0} \right)^{\eta_2}. \tag{17}$$

The redshift z_0 is to the mean redshift of the source galaxy sample, and $\bar{C} = (5 \times 10^{-14}\ h^{-2} M_\odot^{-1} \mathrm{Mpc}^3) \times \rho_{\rm crit}$. The TATT model contains five parameters: the amplitude $A_{i=1,2}$, power law index $\eta_{i=1,2}$, and the effective source galaxy bias b_{TA}. The TATT model reduces to NLA-IA when $A_2 = b_{TA} = 0$. Both NLA-IA and TATT have an explicit dependence on matter density and the growth factor; we assume these are both growth parameters.

IV. DATA AND ANALYSIS METHOD

A. DES data

This work presents results using DES-Y1 and DES-Y3 data; regarding DES-Y1 [69], we have implemented significant changes in the choice of external datasets and nonlinear modeling. In both datasets, the collaboration measured 2PCF via the TreeCorr algorithm [85]. We follow the collaboration choices when applying scale cuts to remove small-scale information. The resulting 3×2 pt data vector contains 457 points for DES-Y1 and 533 points for DES-Y3.

1. Systematics in galaxy clustering and weak lensing

In this section, we summarize the systematics modeling. We mainly follow the DES-Y3 key projects and point out the difference between DES-Y1 and DES-Y3 [16,84].

Galaxy bias: The linear galaxy bias is parametrized by a scalar for each redshift bin, i.e. $b^i(k,z) = b^i$, for five redshift bins. They are marginalized by a conservative prior $\mathcal{U}(0.8, 3.0)$. We do not consider nonlinear galaxy bias in our analysis.

Intrinsic alignment of galaxy: In our analysis, we adopt NLA for DES-Y1 and TATT for DES-Y3; their respective parameters are shown in Tables II and III. We fix the pivot redshift at $z_0 = 0.62$.

Multiplicative shear calibration: We model the shear calibration with a marginalized parameter m^i for each redshift bin, as shown below,

$$\begin{aligned}\xi^{ij}_\pm(\theta) &\to (1+m^i)(1+m^j)\xi^{ij}_\pm(\theta), \\ \gamma^{ij}_t(\theta) &\to (1+m^j)\gamma^{ij}_t(\theta).\end{aligned} \tag{18}$$

DES-Y1 and DES-Y3 have different calibrations from simulations, detailed in Tables II and III.

Photometric redshift uncertainties: We model the uncertainties in photometric redshift distribution for both source and lens galaxies by a shift parameter, Δz^i_x, unique to each redshift bin i, as shown below,

$$n^i_x(z) = \hat{n}^i_x(z - \Delta z^i_x), \qquad x \in \{\text{source}, \text{lens}\}. \tag{19}$$

DES-Y1 priors for Δz_x^i differ from DES-Y3 priors and both are shown in Tables II and III. We do not model stretches in the photometric redshift distribution of lens galaxies by an additional free parameter σ_z^i as in the DES-Y3 key project.

Lensing magnification: As detailed in [16,86], a parameter C_l^i is defined to describe the foreground mass effects on the observed number density of lens galaxies. The expression that modifies Eq. (12) can be found in [78]. The parameter is calibrated from data for each redshift bin and held fixed in our analysis as shown in Table II. This systematic is not considered for the DES-Y1 dataset in this paper.

Nonlocal effects in galaxy-galaxy lensing: For DES-Y3 specifically, we follow the marginalization approach developed in MacCrann *et al.* [87], and we adopt an informative prior of the point-mass parameter $B_i \in \mathrm{Flat}(-5, 5)$. Such systematic is not considered for the DES-Y1 dataset in this paper.

X_{lens} *factor*: A nonphysical parameter X_{lens} was proposed in DES-Y3 to solve the internal inconsistency between galaxy-galaxy lensing and galaxy clustering 2PCF [15]. The two lensing samples, RedMaGiC and MagLim, show discrepancies between the galaxy bias inferred from galaxy-galaxy lensing and galaxy clustering in the DES-Y3 analysis [53,88]. In this work, we adopt RedMaGiC lensing sample with fixed $X_{\mathrm{lens}} = 1$ for both DES-Y1 and DES-Y3. We plan to follow up this work with a detailed comparison between RedMaGiC and MagLim, including marginalization over X_{lens} parameter and recent changes to the RedMaGiC color selection algorithm [53].

B. Priors and external data

The split between growth and geometry information is not unique. Within our choices, we select external probes so that DES-Y3 is the only constraining dataset on growth parameters besides the boundaries of validity of the Euclid Emulator. We do not present DES-only chains as in [69], since they have shown that DES needs to be combined with external data to provide useful constraining power on the difference between geometry and growth parameters. We combine DES with external data described below:

CMBP: Planck 2018 low-ℓ EE polarization data ($\ell < 30$) in combination with the high-ℓ TTTEEE spectra truncated right after the first peak ($35 < \ell < 396$). Our choice removes late-time Integrated Sachs Wolfe information. It also removes CMB lensing effects as the CMB lensing-induced smoothing on the temperature power spectrum only affects constraints on cosmological parameters when including higher acoustic peaks. We find this prior complementary to the compressed CMB likelihood adopted [69]. Our CMB choices are slightly more conservative on n_s and $\Omega_b h^2$, but they do constrain the early-Universe inflationary amplitude A_s.

SNIa: Pantheon type Ia supernovae sample [89]. Type Ia supernovae are a constraint on geometry parameters only; their likelihood does not require knowledge of the large-scale structure. There are, however, lensing magnification effects on the Hubble diagram [90–92] and growth effects on SNIa peculiar velocity distribution [93,94] that will need to be taken into account in future stage IV surveys; for now, we disregard modeling these growth effects. Note that we do not use the local measurement as the prior on H_0 is strongly in tension with other geometry probes [38].

BBN: We use derived constraint on baryon density from astrophysical probe: $100\Omega_b h^2 = 2.208 \pm 0.052$ [95].

BAO: We use baryon acoustic oscillation data from the SDSS DR7 main galaxy sample [96] in combination with the 6dF galaxy survey [97] at $z_{\mathrm{eff}} = 0.15$ and $z_{\mathrm{eff}} = 0.106$ respectively, and the SDSS BOSS DR12 low-z and CMASS combined galaxy samples at $z = 0.38$, 0.51, 0.61 [98]. These constraints come from comparing the observed scale of the BAO feature and the sound horizon. As a distance measurement of the late universe, we consider BAO to be pure geometry information.

To better understand the effects of these external datasets on the final results, we adopt the following three sets of priors:

Prior 1 (P1): Emulator prior + CMBP.
Prior 2 (P2): Emulator prior + SNIa + BAO + BBN.
Prior 3 (All): Emulator prior + CMBP + SNIa + BAO+ BBN.

Table I summarizes our adopted informative priors on the cosmological parameters. Figure 4 compares DES-Y1/Y3-only chains with the uninformative priors adopted by the DES collaboration against our P1 and P2 priors. This figure assumes a ΛCDM model and Halofit for the nonlinear matter power spectrum. Our priors are consistent with DES-only posteriors in all parameters, including σ_8. Since the SNIa + BAO + BBN combination does not provide any information on inflationary parameters, the only limits on A_s and n_s in P2 comes from the Euclid Emulator bounds. Therefore, comparing DES + P1 against DES + P2 chains offers valuable information on how internal DES tensions that shift A_s and n_s affect our results on growth parameters.

Figures 5 and 6 show that the DES-Y1 and DES-Y3 χ^2 distributions are nearly independent of prior P1/P2/*All* choices in both split ΛCDM and *w*CDM models. The priors

TABLE I. Flat priors for the cosmological parameters. We take the priors as in the Euclid Emulator for the parameters $(A_s, n_s, H_0, \Omega_m^{\mathrm{growth}}, w^{\mathrm{growth}})$. We only include the optical depth of reionization, τ, in chains with CMB data.

Cosmological parameters	Prior
Ω_m^{geo}	$\mathrm{Flat}(0.1, 0.9)$
w^{geo}	$\mathrm{Flat}(-3, -0.01)$
$A_s \times 10^9$	$\mathrm{Flat}(1.7, 2.5)$
n_s	$\mathrm{Flat}(0.92, 1.0)$
H_0	$\mathrm{Flat}(61, 73)$
τ	$\mathrm{Flat}(0.01, 0.8)$
$\Omega_m^{\mathrm{growth}}$	$\mathrm{Flat}(0.24, 0.4)$
w^{growth}	$\mathrm{Flat}(-1.7, -0.7)$

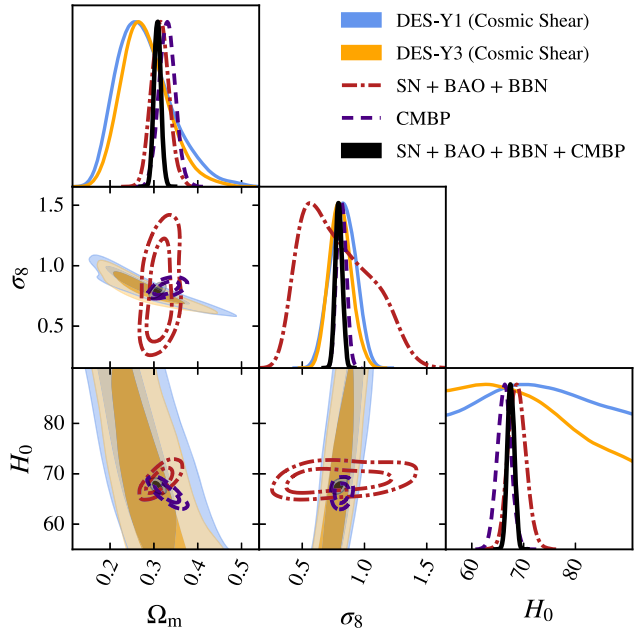

FIG. 4. Cosmic shear posteriors in ΛCDM model for DES-Y1 and DES-Y3. Unlike all remaining figures and results in this manuscript, these constraints assume Halofit for the nonlinear matter power spectrum and the original DES-Y3 priors for the cosmological parameters [15]. The red dot-dashed lines are cosmological constraints from type Ia supernova, BAO and BBN external data. On the other hand, the blue dashed lines show posteriors derived from the cosmic microwave background temperature and polarization Planck 2018 data with the reduced multipole range $35 < \ell < 396$ in combination with low-ℓ EE polarization data $\ell < 30$. These are the external data combinations adopted on priors P2 and P1, respectively (see Sec. IV B). P1 and P2 priors are not stringent enough to create a significant σ_8 tension, but at the same time, they provide complementary information in parameters that DES does not constrain. While both priors measure Ω_m and the Hubble constant H_0, only the CMB data restricts the inflationary parameters A_s and n_s. As shown in Ref. [69], external (non-DES) information is necessary to tightly constrain growth parameters. In comparison with the full TT + low-ℓ EE, the truncated CMB primary here has 3–4 larger standard deviation in A_s and n_s, but Prior 1 + 2 is almost same constraining as full CMB in Ω_m.

are broad enough not to impact the model's DES χ^2 fit, except for the DES-Y3 2 × 2 pt in ΛCDM split. As we will see, the internal tensions on DES-Y3 2 × 2 pt shift the inflationary parameters to values inconsistent with the CMB prior in both ΛCDM and wCDM splits. In ΛCDM, $\Delta\Omega_m$ cannot restore the goodness-of-fit; there is a $\Delta\chi^2 \approx 5$ difference between DES-Y3 2 × 2 pt + P1 and DES-Y3 2 × 2 pt + P2. Interestingly, $\Delta\Omega_m$ and Δw can correct DES-Y3 2 × 2 pt + P1 fit in wCDM split.

C. Pipeline

We perform the MCMC analysis using Cocoa, the Cobaya-CosmoLike Architecture [99]. Cocoa is a modified version of CosmoLike [100] multiprobe analysis software incorporated into the Cobaya framework [101]. DES-Y1 and DES-Y3 covariance matrices were computed using CosmoCov [102]. CosmoCov and Cocoa are both derived from CosmoLike [100], the former pipeline computes covariance matrices, and the latter evaluates data vectors. CosmoLike within Cocoa has efficient OpenMP shared-memory parallelization [103] and cache system compatible with the slow-fast decomposition implemented in the default Cobaya Monte-Carlo Markov chain sampler (MCMC) The OpenMP efficiency in CosmoLike is around 50%; i.e., quadrupling the number of OpenMP cores halves CosmoLike runtime.

CosmoLike has been used in both DES-Y1/Y3 multi-probe analyses when constraining ΛCDM parameters [16,84] and for calibrating Bayesian evidences [104]. It has also been used in forecast studies for Rubin Observatory's LSST and Roman Space Telescope [105–108].

We compute the linear power spectrum with the CAMB Boltzmann code [109,110]; Cobaya already had implementations of all external datasets. We adopt Cobaya's default adaptive metropolis hasting MCMC sampler, and we employ the Gelman-Rubin criteria $R - 1 < 0.02$ to establish chain convergence [111]. We postprocess chains and creat figures using GetDist [112].

Changes in the growth parameters are only semifast; they do not require CAMB to recompute distances and matter power spectrum; only CosmoLike must be rerun to update the DES data vectors. Due to an efficient cache system, CosmoLike reruns with only modified growth parameters takes about half the runtime compared with when all parameters are varied. CAMB and CosmoLike runtimes are roughly equal; the time ratio between slow and semi-fast parameters is, therefore, approximately 4:1. The 3 × 2 pt data vector evaluation time with 10 OpenMP cores is of order 1.5 s on modern AMD EPYC 7642 48-core nodes. This estimation includes CAMB evaluation, non-Limber integration, and TATT modeling. Finally, code comparisons between the CosmoSIS pipeline and CosmoLike were presented in [16,84].

D. Validation on synthetic data

In this section, we generate a synthetic noiseless ΛCDM data vector from *Planck* best fit cosmological parameters without lensing: $\{A_s \times 10^{-9}, n_s, H_0, \Omega_m, \Omega_b\} = \{2.101, 0.965, 67.32, 0.317, 0.049\}$. This set of parameters is compatible with both P1 and P2 priors [113]. We run MCMCs, including all nuisance parameters, and see if the posterior would give equal growth and geometry parameters at the fiducial value.

1. *Comparison between cosmic shear and* 3 × 2 pt

Assuming the All prior and external data combination, there is a significant improvement on $\Omega_m^{\rm growth}$ constraints in ΛCDM split when going from cosmic shear to 3 × 2 pt, as

TABLE II. Adopted priors on DES-Y3 nuisance parameters. The priors are either flat (min, max) or Gaussian (mean, standard deviation).

DES-Y3 nuisance parameters	Prior
Linear galaxy bias	
$b_g^i (i \in [1,5])$	Flat$(0.8, 3.0)$
Intrinsic alignment (TATT)	
A_1	Flat$(-5, 5)$
A_2	Flat$(-5, 5)$
η_1	Flat$(-5, 5)$
η_2	Flat$(-5, 5)$
b_{TA}	Flat$(0, 2)$
Source photo-z	
$\Delta z_s^1 \times 10^2$	Gauss$(0, 1.8)$
$\Delta z_s^2 \times 10^2$	Gauss$(0, 1.5)$
$\Delta z_s^3 \times 10^2$	Gauss$(0, 1.1)$
$\Delta z_s^4 \times 10^2$	Gauss$(0, 1.7)$
Lens photo-z	
$\Delta z_l^1 \times 10^2$	Gauss$(0.6, 0.4)$
$\Delta z_l^2 \times 10^2$	Gauss$(0.1, 0.3)$
$\Delta z_l^3 \times 10^2$	Gauss$(0.4, 0.3)$
$\Delta z_l^4 \times 10^2$	Gauss$(-0.2, 0.5)$
$\Delta z_l^5 \times 10^2$	Gauss$(-0.7, 0.1)$
Multiplicative shear calibration	
$m_1 \times 10^2$	Gauss$(-0.6, 0.9)$
$m_2 \times 10^2$	Gauss$(-2.0, 0.8)$
$m_3 \times 10^2$	Gauss$(-2.4, 0.8)$
$m_4 \times 10^2$	Gauss$(-3.7, 0.8)$
Lens magnification	
$C_l^1 \times 10^2$	Fixed (0.63)
$C_l^2 \times 10^2$	Fixed (-3.04)
$C_l^3 \times 10^2$	Fixed (-1.33)
$C_l^4 \times 10^2$	Fixed (2.50)
$C_l^5 \times 10^2$	Fixed (1.93)
Point mass marginalization	
$B_i (i \in [1,5])$	Flat$(-5, 5)$

TABLE III. Adopted priors on DES-Y1 nuisance parameters. The priors are either flat (min, max) or Gaussian (mean, standard deviation). Note that the parameters not presented here correspond to systematics not considered for DES-Y1 analysis.

DES-Y1 nuisance parameters	Prior
Linear galaxy bias	
$b_g^i (i \in [1,5])$	Flat$(0.8, 3.0)$
Intrinsic alignment (NLA)	
A_1	Flat$(-5, 5)$
η_1	Flat$(-5, 5)$
Source photo-z	
$\Delta z_s^1 \times 10^2$	Gauss$(-0.1, 1.6)$
$\Delta z_s^2 \times 10^2$	Gauss$(-0.19, 1.3)$
$\Delta z_s^3 \times 10^2$	Gauss$(0.9, 1.1)$
$\Delta z_s^4 \times 10^2$	Gauss$(-1.8, 2.2)$
Lens photo-z	
$\Delta z_l^1 \times 10^2$	Gauss$(0.8, 0.7)$
$\Delta z_l^2 \times 10^2$	Gauss$(-0.5, 0.7)$
$\Delta z_l^3 \times 10^2$	Gauss$(0.6, 0.6)$
$\Delta z_l^i \times 10^2 (i \in [4,5])$	Gauss$(0, 0.01)$
Multiplicative shear calibration	
$m_i \times 10^2 (i \in [1,4])$	Gauss$(1.2, 2.3)$

shown in Fig. 7. In the 3×2 pt case, the $\Omega_m^{\rm growth}$ posterior is well centered at the fiducial value, while cosmic shear provides only marginal improvements compared with the uniform $0.24 < \Omega_m^{\rm growth} < 0.4$ prior. This narrow prior is informative in both chains, the boundary coming from the range of the Euclid Emulator. Improving the small-scale modeling validity of cosmic shear and 2×2 pt may tighten the 95% confidence level of $\Omega_m^{\rm growth}$ enough to be within the allowed range; [114,115] offer a roadmap on how to implement such improvements in future work.

DES 3×2 pt combinations with P1 and All external data show nearly identical constraining power on $\Omega_m^{\rm growth}$. Combined priors on the primordial power spectrum (amplitude and shift) and the shape parameter $\Gamma \equiv \Omega_m h$ are the needed external information so that DES can tightly measure growth. The CMBP data alone provide both information while the SNIa + BAO + BBN measurements on $\Omega_m^{\rm geo}$ and H_0 only restrict the shape parameter. Adding more CMB multipoles would improve constraints on early-Universe parameters even more. However, CMB temperature and polarization power spectra are more sensitive to lensing effects on smaller scales, which would limit our ability to compare DES effects on growth parameters against CMB lensing. Partial delensing can alleviate this limitation [116]. Another possibility is to consider all multipoles up to $\ell_{\rm max} \approx 1600$ where effects from nonlinear dark matter collapse are negligible. In this case, however, we would marginalize the chains over lensing principal components so that there is no leakage of information on growth parameters [117].

In the wCDM split model, $\Omega_m^{\rm growth}$ and $w^{\rm growth}$ are not well constrained even in the most informative 3×2 pt case. We then show real data constraints on the principal component combination,

$$\mathrm{PC}_1 = -0.7071 \Delta w + 0.7071 \Delta \Omega_m. \tag{20}$$

In both cosmic shear and 3×2 pt chains, PC_1 constraints are prior dominated but well centered around zero.

2. Comparison between DES-Y1 and DES-Y3

In all three combinations with external data, posteriors on $\Omega_m^{\rm growth}$ in the ΛCDM split from DES-Y1 and DES-Y3 cosmic shear are similar, despite the additional nuisance

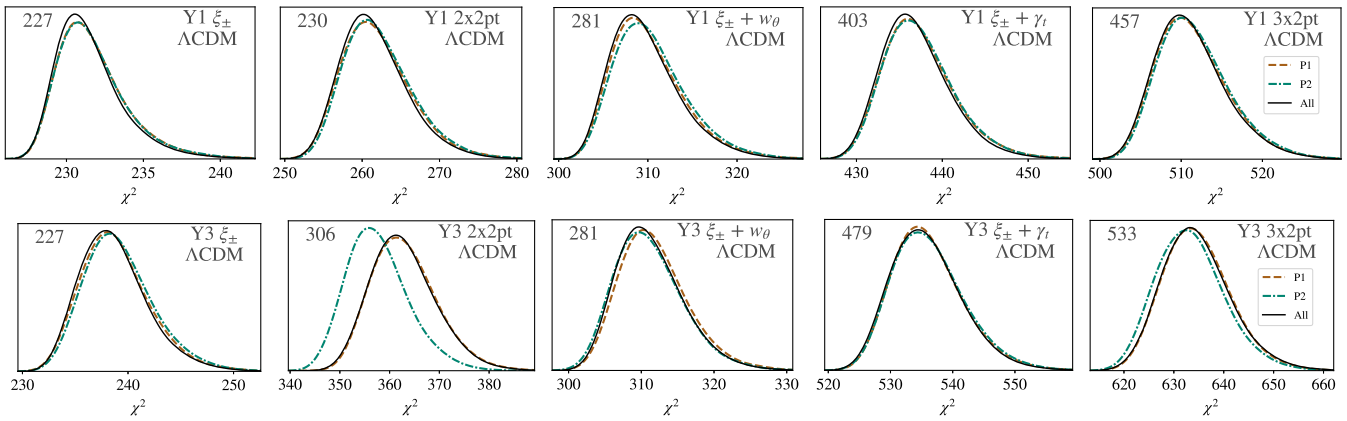

FIG. 5. The DES χ^2 distribution of different combinations of two-point correlation functions in split-ΛCDM chains. The number of data points is printed in the upper left of each panel, after masking us applied for DES-Y1 and DES-Y3, respectively. This plot demonstrates that the P1, P2 and All data priors and external data combinations do not degrade the DES fit except for the DES-Y3 2×2 pt. This anomalous data vector combination predicts a small inflationary amplitude, A_s, in ΛCDM, incompatible with CMB data [15]. The cosmic shear cross-correlation reduces this problem considerably on the 3×2 pt fit. However, the detailed comparison between $\xi_\pm + w_\theta$ and $\xi_\pm + \gamma_t$ against 3×2 pt stands out. Both $\xi_\pm + w_\theta$ and $\xi_\pm + \gamma_t$ combinations show virtually no χ^2 changes between all three priors; the same is not true for 3×2 pt.

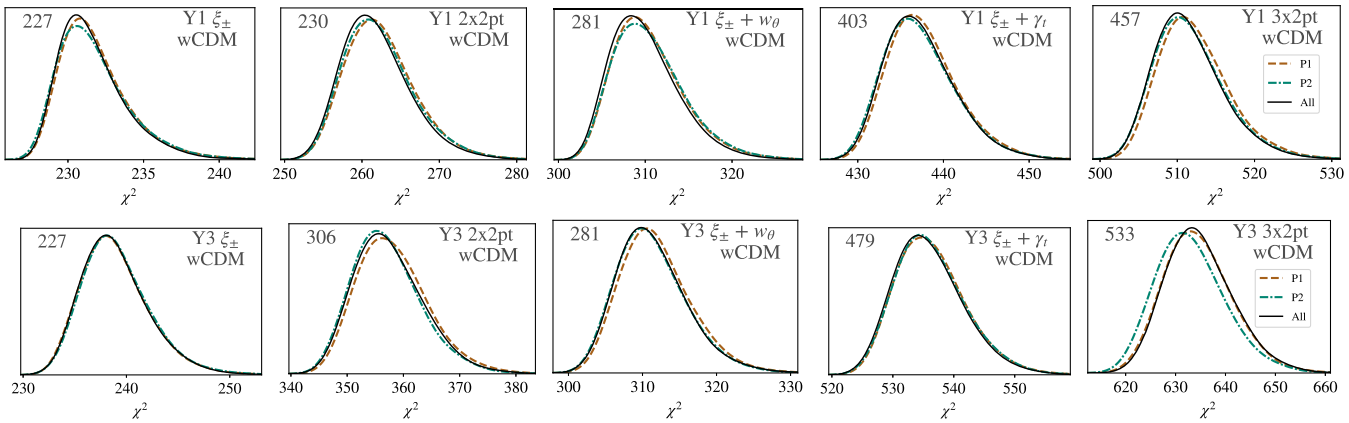

FIG. 6. The DES χ^2 distribution of different combinations of two-point correlation functions in split-wCDM chains. The number of data points is printed in the upper left of each panel, after masking us applied for DES-Y1 and DES-Y3, respectively. This plot demonstrates that the P1, P2 and All data priors and external data combinations do not degrade the DES fit. The 2×2 pt data vector anomalous data vector combination prefers a small inflationary amplitude, A_s in the absence of CMB external data; see Fig. 13. However, growth parameters can restore the DES 2×2 pt goodness-of-fit when A_s is set by the CMB prior, unlike what we observe in the ΛCDM split; see Fig. 5. Indeed, Fig. 13 shows that DES-Y3 2×2 pt data have higher detection of $\Delta\Omega_m - \Delta w < 0$ when combined with CMB data. Unfortunately, both ΛCDM and w-CDM splits have similar goodness-of-fit on the 3×2 pt chains that incorporate cosmic shear, including the slight loss of fit when combining DES and CMB data, and $\Delta\Omega_m - \Delta w$ is consistent with zero.

parameters introduced by the TATT intrinsic alignment model in DES-Y3 (see Fig. 8). We have yet to check if we can obtain more constraining power on growth parameters by adopting the more straightforward NLA model on DES-Y3. On the other hand, the error bar on $\Omega_m^{\rm growth}$ derived from 3×2 pt combined with the All prior is 17% larger in DES-Y1. One caveat to this result is that we have not tested whether expanding the adopted priors on point mass marginalization to the more conservative range $\mathrm{Flat}(-100, 100)$ would significantly degrade DES-Y3 constraints.

The first principle component PC_1, defined on Eq. (20), has nearly identical and prior dominated DES-Y1 and DES-Y3 posteriors in the wCDM split. Additional information from either smaller scales in the 3×2 pt data vector or external growth information from CMB lensing and RSD are potential opportunities in future analyses. Figure 2 shows that $\Omega_m^{\rm growth}$ and $w^{\rm growth}$ induce changes on $\sigma_8^{\rm split}(z)$ with different redshift evolution. Including high redshift $z > 1$ lensing samples from the future Roman Space Telescope may therefore be the key to disentangling growth parameters in wCDM split [107].

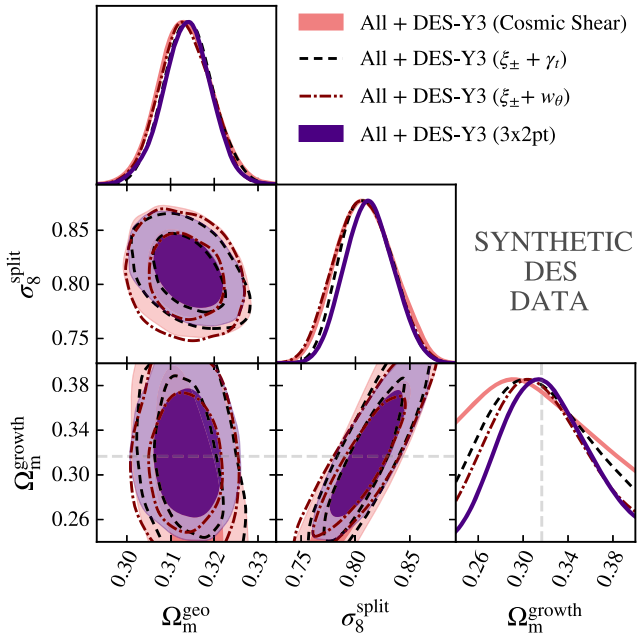

FIG. 7. Posteriors derived from different combinations of synthetic DES-Y3 2PCFs in the split ΛCDM model. As described in Sec. IV B, the All external data combination consists of CMBP + SNIa + BAO + BBN, with CMBP being Planck 2018 low-ℓ EE polarization data and the high-ℓ TTTEEE spectra truncated right after the first peak ($35 < \ell < 396$). Prior to the growth parameter $0.24 \leq \Omega_{\rm m}^{\rm growth} \leq 0.4$ is compatible with the Euclid Emulator boundaries. All posteriors are prior limited, but the plot clarifies the gain in constraining power when galaxy-galaxy lensing and galaxy-clustering are added to cosmic shear.

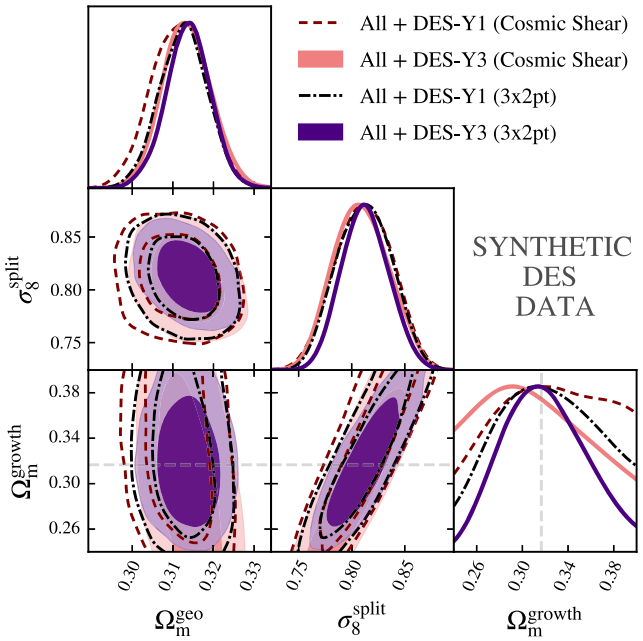

FIG. 8. Split ΛCDM posteriors derived from cosmic shear and 3×2 pt combined with the All external data combination. As described in Sec. IV B, the All external data combination consists of CMBP + SNIa + BAO + BBN, with CMBP being Planck 2018 low-ℓ EE polarization data and the high-ℓ TTTEEE spectra truncated right after the first peak ($35 < \ell < 396$). DES-Y1 3×2 pt error bar on $\Omega_{\rm m}^{\rm growth}$ is approximately 17% larger compared with DES-Y3. On the other hand, cosmic shear DES-Y1 and DES-Y3 constraints are similar, and both are prior dominated.

There are near-future possibilities that may expand the redshift range adopted in this paper. RedMaGiC fifth bin, with range $0.8 < z < 0.9$, shows large $X_{\rm lens}$ biases [115]. The alternative DES-Y3 MagLim sample of lens galaxies does have an additional redshift bin in the range $0.95 < z < 1.05$ not accessible by RedMaGiC [54]. However, MagLim high redshift bins were not adopted in the 3×2 pt analysis by the DES Collaboration and may require further studies on the presence of potential systematic biases [15]. Finally, there is the emergent idea of using the same galaxy sample for both clustering and lensing that could potentially expand DES-Y3 constraints on $\sigma_8^{\rm split}(z)$ beyond $z > 1$ [118].

V. RESULTS

We split our results section into three components: starting with a discussion of our results in the ΛCDM parameter space, we then move to the wCDM space and conclude with quantifying tensions between different probe combinations in the context of both parameter spaces.

A. Growth-geometry split results in ΛCDM

For the most constraining probe combination, DES 3×2 pt + *All*, we show the DES-Y1 and DES-Y3 ΛCDM results in Fig. 9. In both cases we find no measurable detection of $\Delta\Omega_{\rm m}$ being different from zero. This constitutes the main, fiducial result of this paper.

We explore subsets of the 3×2 pt probe combination in Fig. 10, where the left panel refers to DES-Y1 and the right corresponds to DES-Y3. For DES-Y1 we find that in all cases $\Delta\Omega_{\rm m}$ is compatible with zero even within one sigma. For DES-Y3, however, we see shifts from $\Delta\Omega_{\rm m} = 0$, especially in the 2×2 pt (galaxy clustering + galaxy galaxy lensing) case.

We consider this further in Fig. 11, where we show the one-dimensional posterior distributions on all relevant ΛCDM split parameters, finding that except for DES-Y3 $\xi_\pm$ + P2, $\xi_\pm + w_\theta$ and 2×2 pt chains, all combinations of two-point correlation functions predict $\Delta\Omega_{\rm m}$ compatible with zero within one sigma. The deviation on $\xi_\pm$ + P2 is less than two-sigma. Similarly, all combinations between DES 2PCFs and the P2 external data predict $A_{\rm s}$ and $n_{\rm s}$ values compatible with CMB data on P1/*All*, except for DES-Y3 $\xi_\pm + w_\theta$ and 2×2 pt.

Similarly to what we observe in ΛCDM chains with synthetic data vectors, DES-Y1 and DES-Y3 cosmic shear provide little information on $\Delta\Omega_{\rm m}$ even with the P1/P2/*All* priors. The additional nuisance parameters introduced by

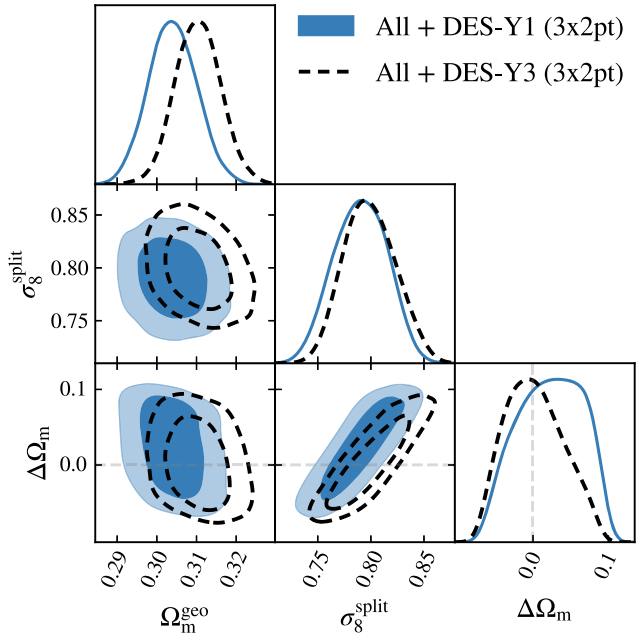

FIG. 9. Split ΛCDM posteriors derived from 3 × 2 pt DES-Y1 and DES-Y3 data. As described in Sec. IV B, the All external data combination consists of CMBP + SNIa + BAO + BBN, with CMBP being Planck 2018 low-ℓ EE polarization data and the high-ℓ TTTEEE spectra truncated right after the first peak ($35 < \ell < 396$). DES-Y1 3 × 2 pt error bar on growth dark matter density is approximately 10% larger compared with DES-Y3.

the TATT intrinsic alignment model and point mass marginalization in DES-Y3 do not reduce constraining power for the growth parameters. The situation in the 3 × 2 pt chains is different; the DES-Y1 3 × 2 pt + *All* error bars are 10% larger than in DES-Y3, not that far from the predicted 17% improvement in the synthetic noise-free chains. Priors on $\Omega_{\rm m}^{\rm growth}$ are still informative, but to a much lesser degree on both DES-Y1 and DES-Y3 3 × 2 pt compared with their cosmic shear counterpart.

All of the DES-Y1 ΛCDM split chains are compatible with $\Delta\Omega_{\rm m} = 0$; Figs. 10 (left panel) and 11 show large consistency between parameter posteriors derived from all 2PCFs combinations. There are also no appreciable parameter shifts between chains with and without CMB priors; goodness-of-fit is identical in these chains (see Fig. 5). As expected, $A_{\rm s}$ and $n_{\rm s}$ constraints are significantly tighter when CMB data are present. Finally, chains that include galaxy clustering (3 × 2 pt, 2 × 2 pt, and $\xi_\pm + w_\theta$) show a small shift towards $\Delta\Omega_{\rm m} > 0$, but are still compatible with zero at 68% confidence level.

For DES-Y3 we see that the $\xi_\pm + w_\theta$ and 2 × 2 pt chains predict, in combination with the All prior, $\Delta\Omega_{\rm m} \neq 0$ at 1.75σ and 2.60σ in statistical significance (see Fig. 10). We attribute these findings to the well-known incompatibilities between galaxy clustering and galaxy-galaxy lensing in DES-Y3 when using the RedMaGiC lens sample.

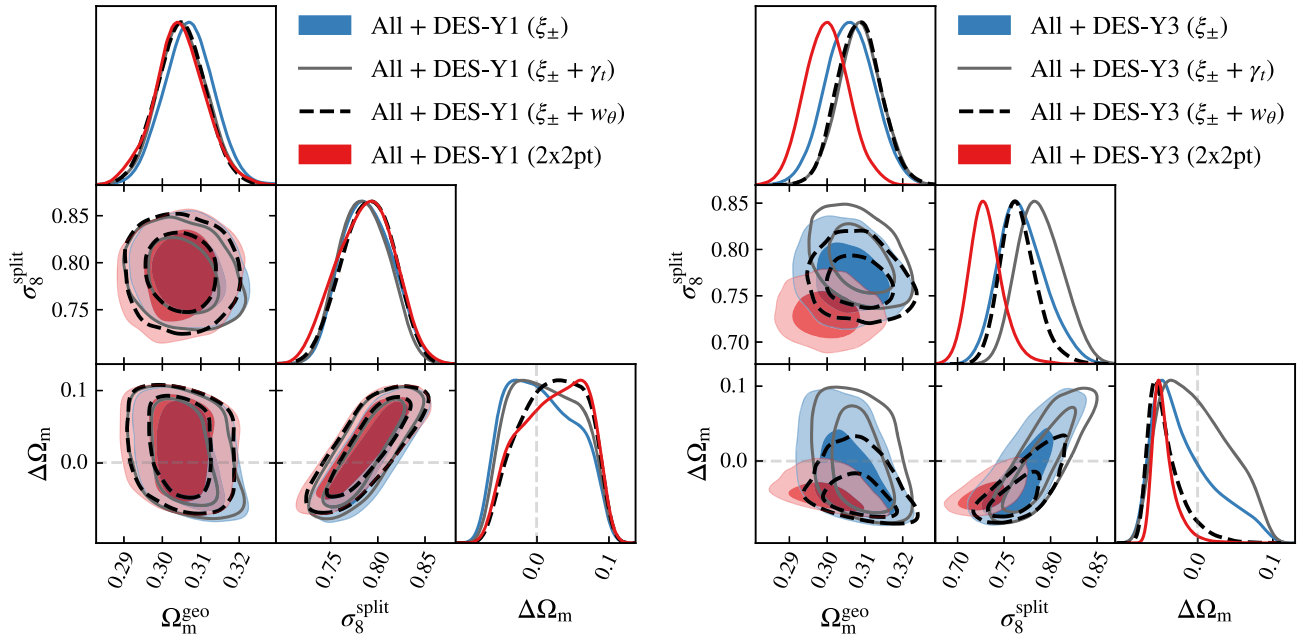

FIG. 10. Split ΛCDM posteriors derived from multiple 2PCF combinations in DES-Y1 (left panel) and DES-Y3 (right panel). As described in Sec. IV B, the All external data combination consists of CMBP + SNIa + BAO + BBN, with CMBP being Planck 2018 low-ℓ EE polarization data and the high-ℓ TTTEEE spectra truncated right after the first peak ($35 < \ell < 396$). Right panel shows that the DES-Y3 $\xi_\pm + \gamma_t$, $\xi_\pm + w(\theta)$ and 2 × 2 pt all prefer lower values for the $\Omega_{\rm m}^{\rm growth}$ with upper limits at 95% confidence level being 0.375, 0.314 and 0.288 respectively. We emphasize that the apparent constraints at $\Delta\Omega_{\rm m} \equiv \Omega_{\rm m}^{\rm growth} - \Omega_{\rm m}^{\rm geo} \approx -0.8$ is due to effective priors.

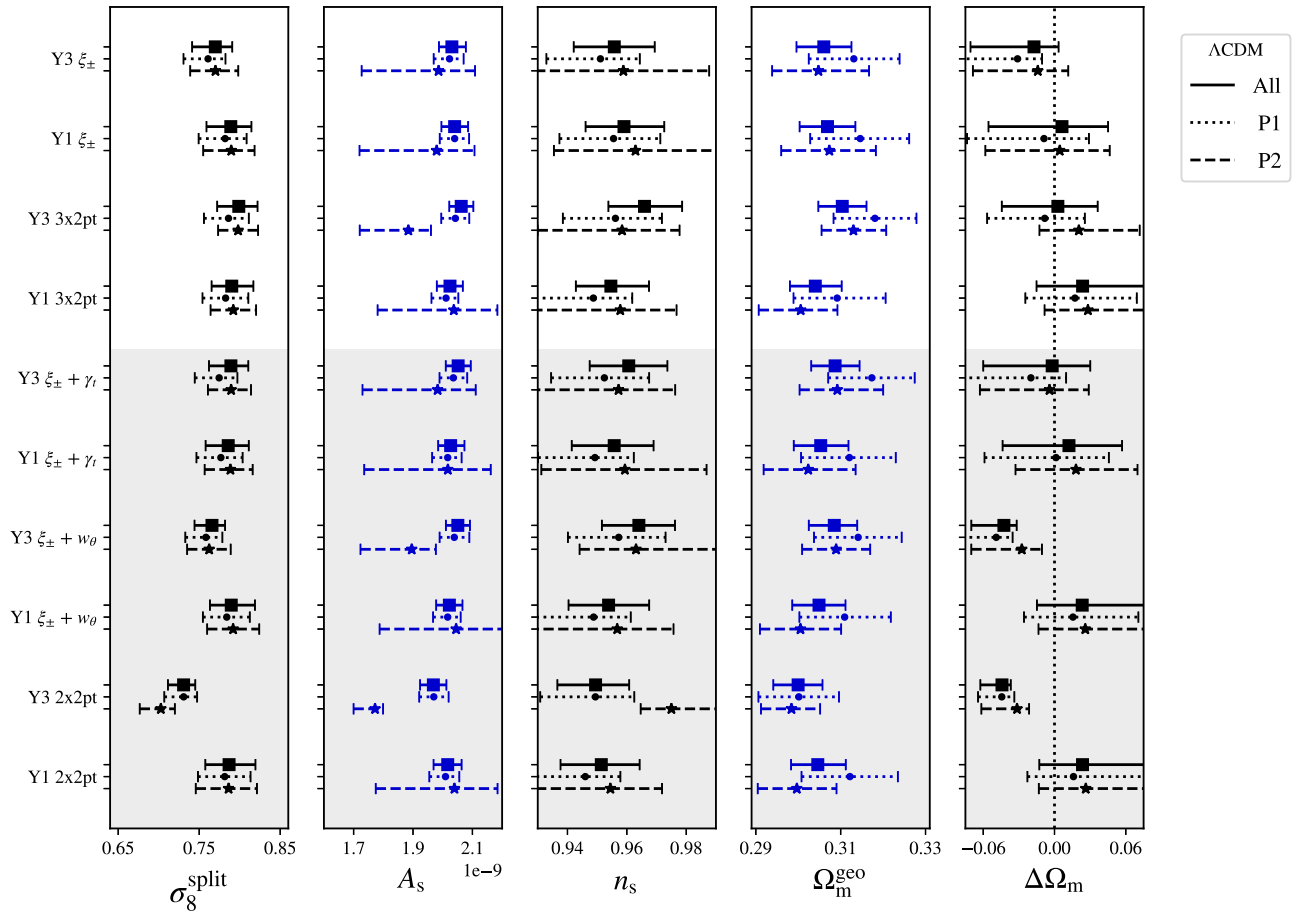

FIG. 11. One-dimensional posteriors in split ΛCDM for various DES-Y1 and DES-Y3 two-point correlation functions, with error bars corresponding to marginalized 68% confidence intervals. As described in Sec. IV B, the All external data combination consists of CMBP + SNIa + BAO + BBN, with CMBP being Planck 2018 low-ℓ EE polarization data and the high-ℓ TTTEEE spectra truncated right after the first peak ($35 < \ell < 396$). The P1 external data combination is restricted to CMBP, while P2 is SNIa + BAO + BBN. Priors on cosmological parameters are summarized in Table I; we define $\Delta\Omega_{\rm m} \equiv \Omega_{\rm m}^{\rm growth} - \Omega_{\rm m}^{\rm geo}$. The gray background separates our primary results from other probe combinations.

B. Growth-geometry split results in *w*CDM

For the *w*CDM parameter space we summarize our results in Figs. 12 and 13, where the former again shows selected results in two dimensions and the latter summarizes all chains in one-dimensional projections. Qualitatively, we see similar behavior as in the ΛCDM case. While DES cosmic shear and 3×2 pt data shows $\Delta\Omega_{\rm m} - \Delta w$ being consistent with zero, the picture becomes more complicated when considering subsets of the 3×2 pt case that involve galaxy clustering of RedMaGiC.

In particular, the 2×2 pt + *All* chain favors $\Delta\Omega_{\rm m} - \Delta w < 0$ at 4.48σ, higher than any $\Delta\Omega_{\rm m} \neq 0$ detection in ΛCDM split. The *w*CDM split 2×2 pt + *All* chain also predict quite low $\sigma_8^{\rm split} = 0.682 \pm 0.0243$, while in ΛCDM we have $\sigma_8^{\rm split} = 0.730 \pm 0.1813$.

While a 4.48σ detection is significant, we again refrain from claiming new physics in the *w*CDM model space, due to the aforementioned problems with the DES-Y3 RedMaGiC sample. Instead, we plan to further investigate growth-geometry split with alternative lens samples and when marginalizing over $X_{\rm lens}$.

C. Quantifying tensions between probes

1. Method

To evaluate the tension we use the parameter difference method [119,120]. Given two chains θ_1 and θ_2 and their corresponding posteriors $\mathcal{P}_1(\theta_1)$ and $\mathcal{P}_2(\theta_2)$, begin by computing the difference between these two chains, denoted with $\Delta\theta = \theta_1 - \theta_2$. Using this difference chain we can write $\mathcal{P}_2(\theta_2) = \mathcal{P}_2(\theta_1 - \Delta\theta)$. By marginalizing over θ_1 we get the parameter difference posterior,

$$\mathcal{P}(\Delta\theta) = \int_{V_\Pi} \mathcal{P}_1(\theta_1)\mathcal{P}_2(\theta_1 - \Delta\theta)d\theta_1, \qquad (21)$$

where V_Π is the subset of the domain covered by the prior. As $\theta_1 \to \theta_2$, the means of each chain approach equality and

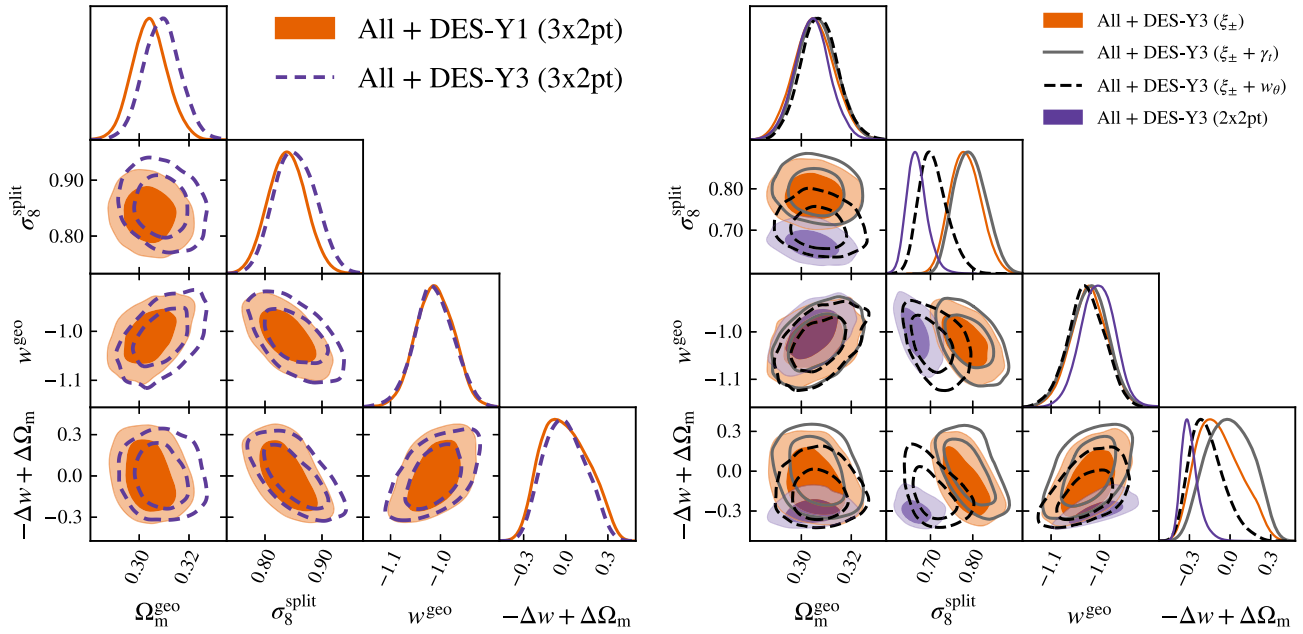

FIG. 12. Split wCDM posteriors derived from 3×2 pt (left panel) and multiple 2PCF combinations (right panel). As described in Sec. IV B, the All external data combination consists of CMBP + SNIa + BAO + BBN, with CMBP being Planck 2018 low-ℓ EE polarization data and the high-ℓ TTTEEE spectra truncated right after the first peak ($35 < \ell < 396$). Table I presents the priors on the cosmological parameters; we define $\Delta\Omega_m \equiv \Omega_m^{growth} - \Omega_m^{geo}$ and $\Delta w \equiv w^{growth} - w^{geo}$. All constraints on the combination $\Delta\Omega_m - \Delta w$ are prior dominated given the range limitations of Ω_m^{growth}.

the mean of the parameter difference chain approaches 0. Thus the volume of the regions with $\mathcal{P}(\Delta\theta) > \mathcal{P}(0)$ approaches 0, so we can approximate the tension using

$$\Delta = \int_{\mathcal{P}(\Delta\theta)>\mathcal{P}(0)} \mathcal{P}(\Delta\theta) d\Delta\theta. \tag{22}$$

This volume is interpreted as a probability of parameter shift, denoted Δ. If Δ comes from a Gaussian distribution, the number of standard deviations from 0 is given by

$$n_\sigma = \sqrt{2}\ \mathrm{Erf}^{-1}(\Delta). \tag{23}$$

The resulting n_σ is reported.

To estimate the posterior we use Masked Autoregressive Flows (MAFs) [119,121], which is a neural network that learns an invertible mapping from an arbitrary parameter space to a Gaussianized one. The loss function for MAFs is the negative log probability from a unit Gaussian. Due to the autoregressive property, the Jacobian is triangular and thus the determinant is tractable to compute even for a large number of dimensions. Thus we can estimate the posterior as a reparametrization of a Gaussian and find the log-probability of arbitrary points.

Before training the neural network, we follow the implementation in Ref. [119] to apply a linear transformation to $\Delta\theta$ given from the Gaussian approximation for $\mathcal{P}(\Delta\theta)$,

$$\Delta\theta' = C^{-1}(\Delta\theta - \mu), \tag{24}$$

with C the covariance and μ the mean of $\mathcal{P}(\Delta\theta)$, then map $\Delta\theta'$ to the fully Gaussianized parameter space. This enhances the convergence rate of the neural networks. Denoting the learned mapping as $\phi(\Delta\theta') = y$ and the unit Gaussian density as $\mathcal{N}$, we can then relate the log-probability as

$$\mathcal{P}(\Delta\theta) = \mathcal{N}(y) \frac{|\det(J_\phi(\Delta\theta'))|}{|\det(C)|}, \tag{25}$$

where J_ϕ denotes the Jacobian of ϕ.

To compute the integral in Eq. (22) we use Monte Carlo integration. Using the MAF we randomly sample from the posterior and calculate the log probability. The fraction of generated points that land in the region $\mathcal{P}(\Delta\theta) > \mathcal{P}(0)$ are counted. The error of the numerical integration is given by the Clopper-Pearson interval for a binomial distribution.

2. Results

We evaluate tensions between different DES 2PCF combinations employing the parameter difference method on $\{A_s, n_s, H_0, \Omega_m^{geo}, \sigma_8^{split}(z=0)\}$ set of cosmological parameters, with an addition of w^{geo} in the split wCDM model. As a caveat, this metric does not model the existing correlations between the 2PCFs; the precise computation requires MCMC chains with repeated parameters, which is

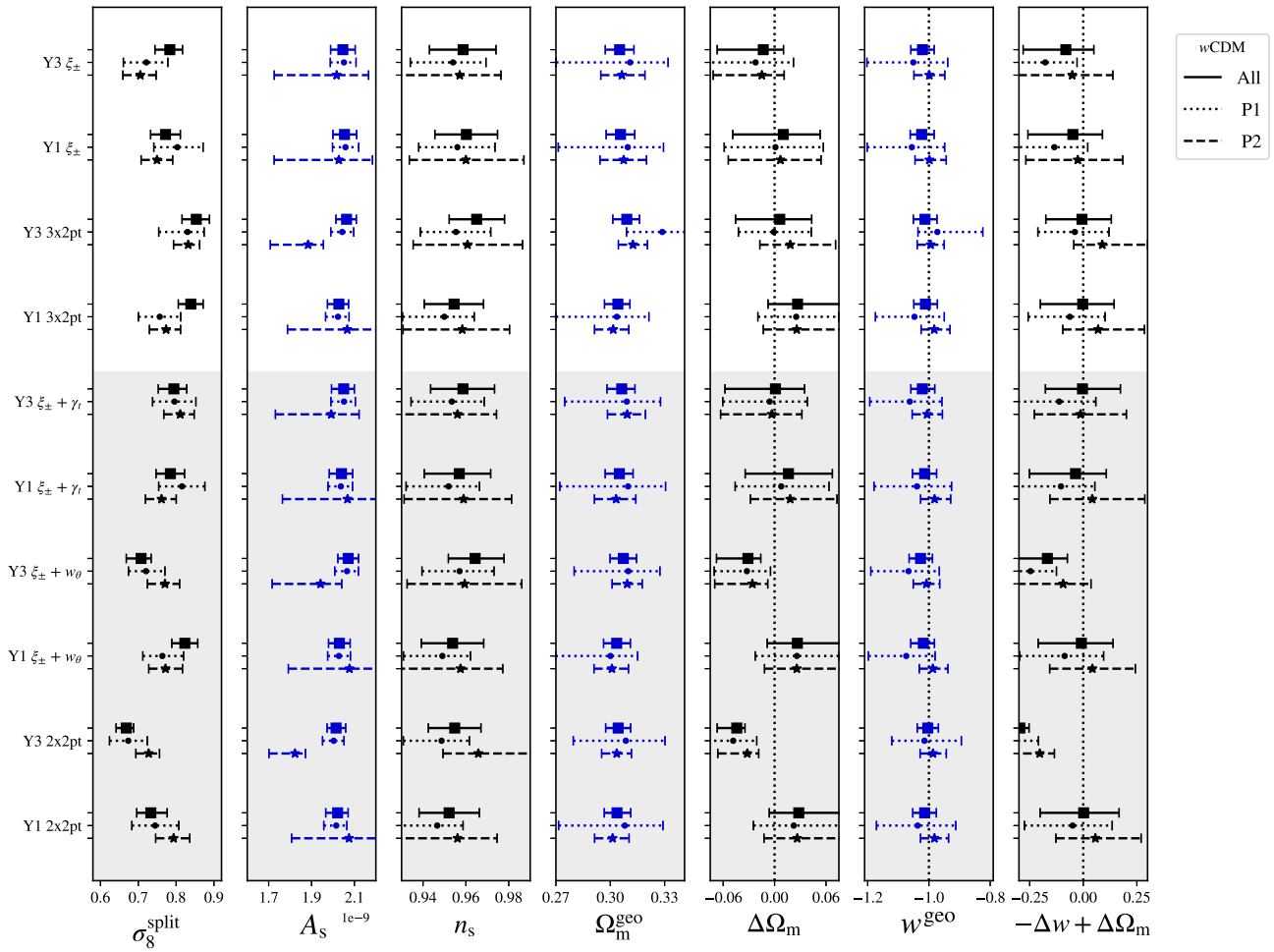

FIG. 13. One-dimensional posteriors in split wCDM for various DES-Y1 and DES-Y3 two-point correlation functions, with error bars corresponding to marginalized 68% confidence intervals. As described in Sec. IV B, the All external data combination consists of CMBP + SNIa + BAO + BBN, with CMBP being Planck 2018 low-ℓ EE polarization data and the high-ℓ TTTEEE spectra truncated right after the first peak ($35 < \ell < 396$). The P1 external data combination is restricted to CMBP, while P2 is SNIa + BAO + BBN. Priors on cosmological parameters are summarized in Table I; we define $\Delta\Omega_{\rm m} \equiv \Omega_{\rm m}^{\rm growth} - \Omega_{\rm m}^{\rm geo}$ and $\Delta w \equiv w^{\rm growth} - w^{\rm geo}$. The gray background separates our primary results from other probe combinations. As could be expected, the DES-Y3 2×2 pt + P2 predicts lower values for the inflationary amplitude $A_{\rm s}$ incompatible with CMB priors. The DES-Y3 2×2 pt also predicts nonzero values for the principal component $\Delta\Omega_{\rm m} - \Delta w$ for all external data combinations; the more extreme deviations being DES-Y3 2×2 pt + ALL with mean -0.296 and standard deviation 0.066.

beyond our computational capabilities [119]. Figure 14 qualitatively indicates discrepancies; we see, for example, the well-known RedMaGiC problems between 2×2 pt and other probe combinations. Future utilization of machine learning emulators will allow the more precise calculation of tensions between the correlated DES 2PCFs with modest computational resources [122].

Interestingly, $A_{\rm s}$ appears to be the culprit of the observed tensions above two sigmas between 2×2 pt and the remaining combinations of the DES-Y3 data vector. The highest observed tension in split ΛCDM happens between 2×2 pt + P2 and $\xi_\pm + w_\theta$ + P1, entirely due to shifts on $A_{\rm s}$ as both chains favors $\Delta\Omega_{\rm m} < 0$. Figure 5 reveals that CMB priors degrade the goodness of fit to DES-Y3 2×2 pt data by $\Delta\chi^2 \approx 5$. In all other DES-Y3 2PCFs, swapping P1 with P2 priors does not affect χ^2 nearly as much. However, the detailed comparison between $\xi_\pm + w_\theta$ and $\xi_\pm + \gamma_t$ against 3×2 pt stands out. Both $\xi_\pm + w_\theta$ and $\xi_\pm + \gamma_t$ combinations show virtually no χ^2 changes between all three priors;the same is not true for 3×2 pt as there is a $\Delta\chi^2 \approx 1.21$ deg radation on DES goodness-of-fit when CMB data is present.

The behavior in wCDM split is different; growth parameters can restore the DES 2×2 pt goodness-of-fit when $A_{\rm s}$ is set by the CMB prior, as shown in Fig. 6. The $A_{\rm s}$ tension between DES-Y3 2×2 pt + P2 and DES-Y3 2×2 pt + P1/*All* is also smaller on wCDM when compared with ΛCDM split. The DES-Y3 2×2 pt predicts

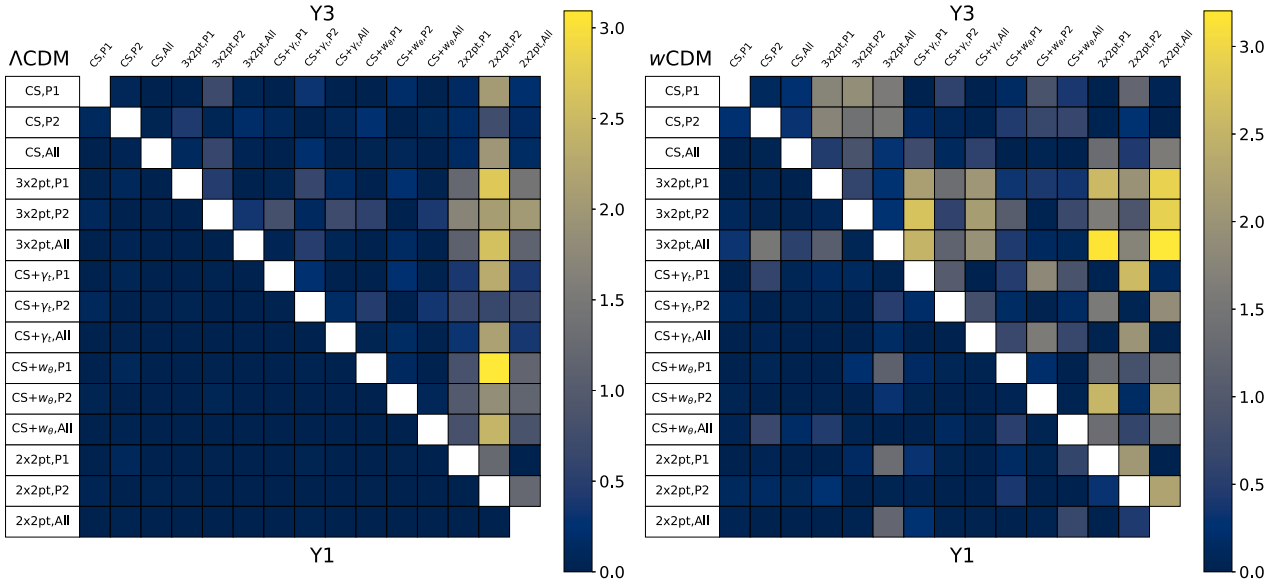

FIG. 14. Tensions between chains under split ΛCDM (left panel) and wCDM (right panel) models. As described in Sec. IV B, the P1 external data combination is composed of Planck 2018 low-ℓ EE polarization data and the high-ℓ TTTEEE spectra truncated right after the first peak ($35 < \ell < 396$). On the other hand, P2 is the combination of SNIa + BAO + BBN. The 2×2 pt + P2 chain is the only one with significant tension, against other DES-Y3 2PCFs, in ΛCDM split; the inflationary amplitude A_s seems to be the culprit of the observed tensions. When 2×2 pt is combined with either P1 or All priors, we see lower tensions at the expense of degradation in goodness-of-fit (see Fig. 5). The wCDM behavior is different; the 2×2 pt + P1/*All* chains have the highest tensions, against 3×2 pt + ALL caused by $\sigma_8^{\rm split}$, and there is no loss in goodness-of-fit compared with 2×2 pt + P2 (see Fig. 6).

nonzero values for the principal component $\Delta\Omega_m - \Delta w$ for all external data combinations, the more extreme deviation from zero happening on DES-Y3 2×2 pt + *All* chain. The better fit to DES 2×2 pt makes such nonzero detection more meaningful than the ΛCDM split model.

Finally, the left and right panels on Fig. 14 show that DES-Y3 2×2 pt + P1/*All* chains have higher tension levels against other 2PCFs than DES-Y3 2×2 pt + P2, the opposite of what we observe in ΛCDM split. Indeed, when cosmic shear is added to 2×2 pt, the predicted $\sigma_8^{\rm split}$ value shifts by more than three sigmas. Unfortunately, both Λ and wCDM split models have similar DES 3×2 pt goodness-of-fit; growth parameters can not alleviate the incompatibility between galaxy-galaxy lensing and galaxy clustering in the 3×2 pt chains (see Figs. 5 and 6).

VI. CONCLUSIONS

This paper studies the growth-geometry split with DES-Y1 and DES-Y3 data in combination with external datasets. We utilize the Cobaya-CosmoLike Architecture (Cocoa) software to efficiently run a large number of MCMC chains that allow us to explore the variation of results for different probes and prior combinations.

For DES-Y1 we find that $\Delta\Omega_m$ in ΛCDM and $\Delta\Omega_m - \Delta w$ in wCDM are both consistent with 0 for all permutations of DES 2PCFs and external prior combinations.

In the case of DES-Y3, we find that cosmic shear and 3×2 pt results are consistent with equal geometry and growth parameters. Combining cosmic shear and galaxy-galaxy lensing also does not indicate deviations between growth and geometry parameters. However, both the $\xi_\pm + w_\theta$ and $\gamma_t + w_\theta$ combinations of 2PCF indicate $\Delta\Omega_m < 0$ in ΛCDM and $\Delta\Omega_m - \Delta w < 0$ in wCDM splits. These results hold with both P1 and P2 priors, which is interesting as they predict different values for the primordial power spectrum amplitude A_s. In light of the well-known DES-Y3 problems of the RedMaGiC sample, we do not interpret these results as a detection but rather assume that it is a residual of unsolved systematics. We plan to further explore this with alternative lens samples, in particular the MagLim sample, and when marginalizing over the $X_{\rm lens}$ [115].

Comparing our work with other results in the literature is unfortunately not straightforward since there are several different ways how ΛCDM parameters can be split into geometry and growth. This work focuses on additional parameters allowing an anomalous late-time growth-independent evolution of the matter power spectrum. In [71], on the other hand, the growth parameters also affect the source function of the CMB power spectrum. Thus, different values of $\Omega_m^{\rm growth}$ affect both early and late-time dynamics and produce significant changes to the CMB temperature and polarization power spectra. These split parametrizations that affect both early and late-time dynamics produce $\Delta\Omega_m \neq 0$ detections at a level greater than 4σ, much higher than what we observe with our adopted late-time scale-independent modifications to the matter power spectrum.

References [123,124] describe a third possibility for the split. Their growth parameters affect the growth index γ, which is a single parameter that approximately describes the ΛCDM growth history in the late Universe.

Several extensions to this paper come to mind: Firstly, we already mentioned that it will be important to study the impact of other lens samples, in particular the MagLim sample. Secondly, additional cosmological information from external datasets, such as including more scales of the CMB temperature and polarization power spectrum, and adding CMB lensing are near-term extensions of this work. The wCDM split would also benefit from extra information on $w^{\rm geo}$ from the observed DES type IA supernova included in the new Phanteon+ sample [125]. Thirdly, we plan to include small-scale information to increase the constraining power on growth-geometry split parameters, e.g. by modeling baryons in cosmic shear as in [114] or modeling galaxy bias in 2×2 pt via effective field theory [126] or via Halo Occupation Distribution models [100,127,128].

While this paper does not show any hints of new physics beyond ΛCDM, future datasets from Rubin Observatory's LSST [129], the Roman Space Telescope [130], and the Euclid mission [131], in combination with the Dark Energy Spectroscopic Instrument [132], Simons Observatory [133] and the CMB-S4 mission [134] will significantly tighten the statistical error budget on cosmological models beyond ΛCDM and wCDM. It is now timely to develop the theoretical toolbox to efficiently and consistently explore these models across datasets.

ACKNOWLEDGMENTS

Simulations in this paper use High Performance Computing (HPC) resources supported by the University of Arizona Technology and Research Initiative Fund (TRIF) and maintained by the UA Research Technologies department. The authors would also like to thank Stony Brook Research Computing and Cyberinfrastructure, and the Institute for Advanced Computational Science at Stony Brook University for access to the high-performance SeaWulf computing system, which was made possible by a $1.4 M National Science Foundation grant (1531492). T. E. and J. X. are supported by the Department of Energy grant DE-SC0020215. E. K. is supported by the Department of Energy grant DESC0020247 and an Alfred P. Sloan Research Fellowship.

[1] A. G. Riess, A. V. Filippenko, P. Challis, A. Clocchiatti, A. Diercks, P. M. Garnavich, R. L. Gilliland, C. J. Hogan, S. Jha, R. P. Kirshner *et al.*, Astron. J. **116**, 1009 (1998).
[2] S. Perlmutter, G. Aldering, G. Goldhaber, R. A. Knop, P. Nugent, P. G. Castro, S. Deustua, S. Fabbro, A. Goobar, D. E. Groom *et al.*, Astrophys. J. **517**, 565 (1999).
[3] S. Weinberg, Rev. Mod. Phys. **61**, 1 (1989).
[4] R. R. Caldwell, R. Dave, and P. J. Steinhardt, Phys. Rev. Lett. **80**, 1582 (1998).
[5] I. Zlatev, L. Wang, and P. J. Steinhardt, Phys. Rev. Lett. **82**, 896 (1999).
[6] S. Tsujikawa, Classical Quantum Gravity **30**, 214003 (2013).
[7] C. Armendariz-Picon, V. F. Mukhanov, and P. J. Steinhardt, Phys. Rev. D **63**, 103510 (2001).
[8] Y.-F. Cai, E. N. Saridakis, M. R. Setare, and J.-Q. Xia, Phys. Rep. **493**, 1 (2010).
[9] S. Tsujikawa, in *Lectures on Cosmology*, edited by G. Wolschin (Springer, Berlin, Heidelberg, 2010), Vol. 800, pp. 99–145.
[10] T. Abbott, F. B. Abdalla, J. Aleksić, S. Allam, A. Amara, D. Bacon, E. Balbinot, M. Banerji, K. Bechtol *et al.* (Dark Energy Survey Collaboration), Mon. Not. R. Astron. Soc. **460**, 1270 (2016).
[11] T. M. C. Abbott, F. B. Abdalla, A. Alarcon, J. Aleksić, S. Allam, S. Allen, A. Amara, J. Annis, J. Asorey, S. Avila *et al.*, Phys. Rev. D **98**, 043526 (2018).
[12] M. A. Troxel, N. MacCrann, J. Zuntz, T. F. Eifler, E. Krause, S. Dodelson, D. Gruen, J. Blazek, O. Friedrich, S. Samuroff *et al.*, Phys. Rev. D **98**, 043528 (2018).
[13] Y. Omori, E. J. Baxter, C. Chang, D. Kirk, A. Alarcon, G. M. Bernstein, L. E. Bleem, R. Cawthon, A. Choi, R. Chown *et al.*, Phys. Rev. D **100**, 043517 (2019).
[14] T. M. C. Abbott, M. Aguena, A. Alarcon, S. Allam, S. Allen, J. Annis, S. Avila, D. Bacon, K. Bechtol, A. Bermeo *et al.*, Phys. Rev. D **102**, 023509 (2020).
[15] T. M. C. Abbott, M. Aguena, A. Alarcon, S. Allam, O. Alves, A. Amon, F. Andrade-Oliveira, J. Annis, S. Avila, D. Bacon *et al.*, Phys. Rev. D **105**, 023520 (2022).
[16] E. Krause, X. Fang, S. Pandey, L. F. Secco, O. Alves, H. Huang, J. Blazek, J. Prat, J. Zuntz, T. F. Eifler *et al.*, arXiv:2105.13548.
[17] T. M. C. Abbott, M. Aguena, A. Alarcon, O. Alves, A. Amon, J. Annis, S. Avila, D. Bacon, E. Baxter *et al.* (DES Collaboration), Phys. Rev. D **107**, 083504 (2023).
[18] A. Amon, D. Gruen, M. A. Troxel, N. MacCrann, S. Dodelson, A. Choi, C. Doux, L. F. Secco, S. Samuroff, E. Krause *et al.*, Phys. Rev. D **105**, 023514 (2022).
[19] K. Kuijken, C. Heymans, H. Hildebrandt, R. Nakajima, T. Erben, J. T. A. de Jong, M. Viola, A. Choi, H. Hoekstra, L. Miller *et al.*, Mon. Not. R. Astron. Soc. **454**, 3500 (2015).
[20] S. Joudaki, H. Hildebrandt, D. Traykova, N. E. Chisari, C. Heymans, A. Kannawadi, K. Kuijken, A. H. Wright, M. Asgari, T. Erben *et al.*, Astron. Astrophys. **638**, L1 (2020).
[21] C. Heymans, T. Tröster, M. Asgari, C. Blake, H. Hildebrandt, B. Joachimi, K. Kuijken, C.-A. Lin,

A. G. Sánchez, J. L. van den Busch *et al.*, Astron. Astrophys. **646**, A140 (2021).
[22] M. Asgari, C.-A. Lin, B. Joachimi, B. Giblin, C. Heymans, H. Hildebrandt, A. Kannawadi, B. Stölzner, T. Tröster, J. L. van den Busch *et al.*, Astron. Astrophys. **645**, A104 (2021).
[23] J. Ruiz-Zapatero, B. Stölzner, B. Joachimi, M. Asgari, M. Bilicki, A. Dvornik, B. Giblin, C. Heymans, H. Hildebrandt, A. Kannawadi *et al.*, Astron. Astrophys. **655**, A11 (2021).
[24] H. Aihara, N. Arimoto, R. Armstrong, S. Arnouts, N. A. Bahcall, S. Bickerton, J. Bosch, K. Bundy, P. L. Capak, J. H. H. Chan *et al.*, Publ. Astron. Soc. Jpn. **70**, S4 (2018).
[25] C. Hikage, M. Oguri, T. Hamana, S. More, R. Mandelbaum, M. Takada, F. Köhlinger, H. Miyatake, A. J. Nishizawa, H. Aihara *et al.*, Publ. Astron. Soc. Jpn. **71**, 43 (2019).
[26] T. Hamana, M. Shirasaki, S. Miyazaki, C. Hikage, M. Oguri, S. More, R. Armstrong, A. Leauthaud, R. Mandelbaum, H. Miyatake *et al.*, Publ. Astron. Soc. Jpn. **72**, 16 (2020).
[27] M. M. Rau, R. Dalal, T. Zhang, X. Li, A. J. Nishizawa, S. More, R. Mandelbaum, M. A. Strauss, and M. Takada, arXiv:2211.16516.
[28] H. Aihara, Y. AlSayyad, M. Ando, R. Armstrong, J. Bosch, E. Egami, H. Furusawa, J. Furusawa, S. Harasawa, Y. Harikane *et al.*, Publ. Astron. Soc. Jpn. **74**, 247 (2022).
[29] S. A. Smee, J. E. Gunn, A. Uomoto, N. Roe, D. Schlegel, C. M. Rockosi, M. A. Carr, F. Leger, K. S. Dawson, M. D. Olmstead *et al.*, Astron. J. **146**, 32 (2013).
[30] K. S. Dawson, J.-P. Kneib, W. J. Percival, S. Alam, F. D. Albareti, S. F. Anderson, E. Armengaud, É. Aubourg, S. Bailey, J. E. Bautista *et al.*, Astron. J. **151**, 44 (2016).
[31] S. Alam, M. Aubert, S. Avila, C. Balland, J. E. Bautista, M. A. Bershady, D. Bizyaev, M. R. Blanton, A. S. Bolton, J. Bovy *et al.*, Phys. Rev. D **103**, 083533 (2021).
[32] G. Merz, M. Rezaie, H.-J. Seo, R. Neveux, A. J. Ross, F. Beutler, W. J. Percival, E. Mueller, H. Gil-Marín, G. Rossi *et al.*, Mon. Not. R. Astron. Soc. **506**, 2503 (2021).
[33] C. Zhao, A. Variu, M. He, D. Forero-Sánchez, A. Tamone, C.-H. Chuang, F.-S. Kitaura, C. Tao, J. Yu, J.-P. Kneib *et al.*, Mon. Not. R. Astron. Soc. **511**, 5492 (2022).
[34] M. J. Chapman, F. G. Mohammad, Z. Zhai, W. J. Percival, J. L. Tinker, J. E. Bautista, J. R. Brownstein, E. Burtin, K. S. Dawson, H. Gil-Marín *et al.*, Mon. Not. R. Astron. Soc. **516**, 617 (2022).
[35] M. Douspis, L. Salvati, and N. Aghanim, Proc. Sci. EDSU2018 (**2018**) 037 [arXiv:1901.05289].
[36] A. G. Riess, S. Casertano, W. Yuan, L. M. Macri, and D. Scolnic, Astrophys. J. **876**, 85 (2019).
[37] K. C. Wong, S. H. Suyu, G. C. F. Chen, C. E. Rusu, M. Millon, D. Sluse, V. Bonvin, C. D. Fassnacht, S. Taubenberger, M. W. Auger *et al.*, Mon. Not. R. Astron. Soc. **498**, 1420 (2020).
[38] A. G. Riess, W. Yuan, L. M. Macri, D. Scolnic, D. Brout, S. Casertano, D. O. Jones, Y. Murakami, G. S. Anand, L. Breuval *et al.*, Astrophys. J. Lett. **934**, L7 (2022).
[39] K. C. Wong, S. H. Suyu, G. C. F. Chen, C. E. Rusu, M. Millon, D. Sluse, V. Bonvin, C. D. Fassnacht, S. Taubenberger, M. W. Auger *et al.*, Mon. Not. R. Astron. Soc. **498**, 1420 (2020).
[40] A. G. Riess, Nat. Rev. Phys. **2**, 10 (2019).
[41] P. A. R. Ade, N. Aghanim, M. Arnaud, M. Ashdown, J. Aumont, C. Baccigalupi, A. J. Banday, R. B. Barreiro, J. G. Bartlett *et al.* (Planck Collaboration), Astron. Astrophys. **594**, A13 (2016).
[42] N. Aghanim, Y. Akrami, M. Ashdown, J. Aumont, C. Baccigalupi, M. Ballardini, A. J. Banday, R. B. Barreiro, N. Bartolo *et al.* (Planck Collaboration), Astron. Astrophys. **641**, A6 (2020).
[43] W. Hu, ASP Conf. Ser. **339**, 215 (2005), https://ui.adsabs.harvard.edu/abs/2005ASPC..339..215H/abstract.
[44] P. A. R. Ade, N. Aghanim, M. Arnaud, M. Ashdown, J. Aumont, C. Baccigalupi, A. J. Banday, R. B. Barreiro, N. Bartolo *et al.* (Planck Collaboration), Astron. Astrophys. **594**, A14 (2016).
[45] K. L. Pandey, T. Karwal, and S. Das, J. Cosmol. Astropart. Phys. 07 (2020) 026.
[46] S. J. Clark, K. Vattis, and S. M. Koushiappas, Phys. Rev. D **103**, 043014 (2021).
[47] G. E. Addison, D. J. Watts, C. L. Bennett, M. Halpern, G. Hinshaw, and J. L. Weiland, Astrophys. J. **853**, 119 (2018).
[48] P. Lemos, E. Lee, G. Efstathiou, and S. Gratton, Mon. Not. R. Astron. Soc. **483**, 4803 (2019).
[49] S. Dhawan, D. Brout, D. Scolnic, A. Goobar, A. G. Riess, and V. Miranda, Astrophys. J. **894**, 54 (2020).
[50] L. Verde, T. Treu, and A. G. Riess, Nat. Astron. **3**, 891 (2019).
[51] L. Knox and M. Millea, Phys. Rev. D **101**, 043533 (2020).
[52] J. Elvin-Poole, M. Crocce, A. J. Ross, T. Giannantonio, E. Rozo, E. S. Rykoff, S. Avila, N. Banik, J. Blazek, S. L. Bridle *et al.*, Phys. Rev. D **98**, 042006 (2018).
[53] S. Pandey, E. Krause, J. DeRose, N. MacCrann, B. Jain, M. Crocce, J. Blazek, A. Choi, H. Huang, C. To *et al.*, Phys. Rev. D **106**, 043520 (2022).
[54] A. Porredon, M. Crocce, J. Elvin-Poole, R. Cawthon, G. Giannini, J. De Vicente, A. Carnero Rosell, I. Ferrero, E. Krause, X. Fang *et al.*, Phys. Rev. D **106**, 103530 (2022).
[55] A. B. Mantz, A. von der Linden, S. W. Allen, D. E. Applegate, P. L. Kelly, R. G. Morris, D. A. Rapetti, R. W. Schmidt, S. Adhikari, M. T. Allen *et al.*, Mon. Not. R. Astron. Soc. **446**, 2205 (2015).
[56] H. Hildebrandt, M. Viola, C. Heymans, S. Joudaki, K. Kuijken, C. Blake, T. Erben, B. Joachimi, D. Klaes, L. Miller *et al.*, Mon. Not. R. Astron. Soc. **465**, 1454 (2017).
[57] L. F. Secco, T. Karwal, W. Hu, and E. Krause, Phys. Rev. D **107**, 083532 (2023).
[58] J. C. Hill, E. McDonough, M. W. Toomey, and S. Alexander, Phys. Rev. D **102**, 043507 (2020).
[59] M. M. Ivanov, E. McDonough, J. C. Hill, M. Simonović, M. W. Toomey, S. Alexander, and M. Zaldarriaga, Phys. Rev. D **102**, 103502 (2020).
[60] G. D'Amico, L. Senatore, P. Zhang, and H. Zheng, J. Cosmol. Astropart. Phys. 05 (2021) 072.
[61] S. Wang, L. Hui, M. May, and Z. Haiman, Phys. Rev. D **76**, 063503 (2007).
[62] M. J. Mortonson, W. Hu, and D. Huterer, Phys. Rev. D **79**, 023004 (2009).

[63] M. J. Mortonson, W. Hu, and D. Huterer, Phys. Rev. D **81**, 063007 (2010).
[64] E. J. Ruiz and D. Huterer, Phys. Rev. D **91**, 063009 (2015).
[65] V. Miranda and C. Dvorkin, Phys. Rev. D **98**, 043537 (2018).
[66] M. Chu and L. Knox, Astrophys. J. **620**, 1 (2005).
[67] A. Abate and O. Lahav, Mon. Not. R. Astron. Soc. **389**, L47 (2008).
[68] T. L. Smith, V. Poulin, J. L. Bernal, K. K. Boddy, M. Kamionkowski, and R. Murgia, Phys. Rev. D **103**, 123542 (2021).
[69] J. Muir, E. Baxter, V. Miranda, C. Doux, A. Ferté, C. D. Leonard, D. Huterer, B. Jain, P. Lemos, M. Raveri *et al.*, Phys. Rev. D **103**, 023528 (2021).
[70] J. L. Bernal, L. Verde, and A. J. Cuesta, J. Cosmol. Astropart. Phys. 02 (2016) 059.
[71] U. Andrade, D. Anbajagane, R. von Marttens, D. Huterer, and J. Alcaniz, J. Cosmol. Astropart. Phys. 11 (2021) 014.
[72] M. Ishak, A. Upadhye, and D. N. Spergel, Phys. Rev. D **74**, 043513 (2006).
[73] D. Huterer and E. V. Linder, Phys. Rev. D **75**, 023519 (2007).
[74] M. J. Mortonson, D. Huterer, and W. Hu, Phys. Rev. D **82**, 063004 (2010).
[75] A. Lewis, A. Challinor, and A. Lasenby, Astrophys. J. **538**, 473 (2000).
[76] C. Howlett, A. Lewis, A. Hall, and A. Challinor, J. Cosmol. Astropart. Phys. 04 (2012) 027.
[77] M. Knabenhans, J. Stadel, D. Potter, J. Dakin, S. Hannestad, T. Tram, S. Marelli, A. Schneider, R. Teyssier *et al.* (Euclid Collaboration), Mon. Not. R. Astron. Soc. **505**, 2840 (2021).
[78] X. Fang, E. Krause, T. Eifler, and N. MacCrann, J. Cosmol. Astropart. Phys. 05 (2020) 010.
[79] D. N. Limber, Astrophys. J. **117**, 134 (1953).
[80] M. LoVerde and N. Afshordi, Phys. Rev. D **78**, 123506 (2008).
[81] M. Bartelmann and P. Schneider, Phys. Rep. **340**, 291 (2001).
[82] A. Stebbins, arXiv:astro-ph/9609149.
[83] J. Blazek, N. MacCrann, M. A. Troxel, and X. Fang, Phys. Rev. D **100**, 103506 (2019).
[84] E. Krause, T. F. Eifler, J. Zuntz, O. Friedrich, M. A. Troxel, S. Dodelson, J. Blazek, L. F. Secco, N. MacCrann, E. Baxter *et al.*, arXiv:1706.09359.
[85] M. Jarvis, G. Bernstein, and B. Jain, Mon. Not. R. Astron. Soc. **352**, 338 (2004).
[86] J. Elvin-Poole, N. MacCrann, S. Everett, J. Prat, E. S. Rykoff, J. De Vicente, B. Yanny, K. Herner, A. Ferté, E. Di Valentino *et al.*, arXiv:2209.09782.
[87] N. MacCrann, J. Blazek, B. Jain, and E. Krause, Mon. Not. R. Astron. Soc. **491**, 5498 (2020).
[88] T. M. C. Abbott, M. Aguena, A. Alarcon, O. Alves, A. Amon, F. Andrade-Oliveira, J. Annis, B. Ansarinejad, S. Avila, D. Bacon *et al.*, Phys. Rev. D **107**, 023531 (2023).
[89] D. M. Scolnic, D. O. Jones, A. Rest, Y. C. Pan, R. Chornock, R. J. Foley, M. E. Huber, R. Kessler, G. Narayan, A. G. Riess *et al.*, Astrophys. J. **859**, 101 (2018).
[90] Y. Wang, J. Cosmol. Astropart. Phys. 03 (2005) 005.
[91] Z. Zhai and Y. Wang, Phys. Rev. D **99**, 083525 (2019).
[92] Z. Zhai, Y. Wang, and D. Scolnic, Phys. Rev. D **102**, 123513 (2020).
[93] T. Castro, M. Quartin, and S. Benitez-Herrera, Phys. Dark Universe **13**, 66 (2016).
[94] K. Garcia, M. Quartin, and B. B. Siffert, Phys. Dark Universe **29**, 100519 (2020).
[95] T. M. C. Abbott, F. B. Abdalla, J. Annis, K. Bechtol, J. Blazek, B. A. Benson, R. A. Bernstein, G. M. Bernstein, E. Bertin, D. Brooks *et al.*, Mon. Not. R. Astron. Soc. **480**, 3879 (2018).
[96] A. J. Ross, L. Samushia, C. Howlett, W. J. Percival, A. Burden, and M. Manera, Mon. Not. R. Astron. Soc. **449**, 835 (2015).
[97] F. Beutler, C. Blake, M. Colless, D. H. Jones, L. Staveley-Smith, L. Campbell, Q. Parker, W. Saunders, and F. Watson, Mon. Not. R. Astron. Soc. **416**, 3017 (2011).
[98] S. Alam, M. Ata, S. Bailey, F. Beutler, D. Bizyaev, J. A. Blazek, A. S. Bolton, J. R. Brownstein, A. Burden, C.-H. Chuang *et al.*, Mon. Not. R. Astron. Soc. **470**, 2617 (2017).
[99] Cocoa—Cobaya-CosmoLike Joint Architecture, https://github.com/CosmoLike/cocoa (accessed: 2020-10-17).
[100] E. Krause and T. Eifler, Mon. Not. R. Astron. Soc. **470**, 2100 (2017).
[101] J. Torrado and A. Lewis, J. Cosmol. Astropart. Phys. 05 (2021) 057.
[102] X. Fang, T. Eifler, and E. Krause, Mon. Not. R. Astron. Soc. **497**, 2699 (2020).
[103] OpenMP, https://www.openmp.org (accessed: 2020-10-17).
[104] V. Miranda, P. Rogozenski, and E. Krause, Mon. Not. R. Astron. Soc. **509**, 5218 (2021).
[105] T. Eifler, E. Krause, P. Schneider, and K. Honscheid, Mon. Not. R. Astron. Soc. **440**, 1379 (2014).
[106] T. Eifler, H. Miyatake, E. Krause, C. Heinrich, V. Miranda, C. Hirata, J. Xu, S. Hemmati, M. Simet, P. Capak *et al.*, Mon. Not. R. Astron. Soc. **507**, 1746 (2021).
[107] T. Eifler, M. Simet, E. Krause, C. Hirata, H.-J. Huang, X. Fang, V. Miranda, R. Mandelbaum, C. Doux, C. Heinrich *et al.*, Mon. Not. R. Astron. Soc. **507**, 1514 (2021).
[108] R. Mandelbaum, T. Eifler, R. Hložek, T. Collett, E. Gawiser, D. Scolnic, D. Alonso, H. Awan, R. Biswas *et al.* (The LSST Dark Energy Science Collaboration), arXiv:1809.01669.
[109] A. Lewis and S. Bridle, Phys. Rev. D **66**, 103511 (2002).
[110] C. Howlett, A. Lewis, A. Hall, and A. Challinor, J. Cosmol. Astropart. Phys. 04 (2012) 027.
[111] A. Gelman and D. B. Rubin, Stat. Sci. **7**, 457 (1992).
[112] A. Lewis, arXiv:1910.13970.
[113] N. Aghanim, Y. Akrami, F. Arroja, M. Ashdown, J. Aumont, C. Baccigalupi, M. Ballardini, A. J. Banday, R. B. Barreiro *et al.* (Planck Collaboration), Astron. Astrophys. **641**, A1 (2020).
[114] H.-J. Huang, T. Eifler, R. Mandelbaum, G. M. Bernstein, A. Chen, A. Choi, J. García-Bellido, D. Huterer, E. Krause, E. Rozo *et al.*, Mon. Not. R. Astron. Soc. **502**, 6010 (2021).
[115] S. Pandey, E. Krause, J. DeRose, N. MacCrann, B. Jain, M. Crocce, J. Blazek, A. Choi, H. Huang, C. To *et al.*, Phys. Rev. D **106**, 043520 (2022).

[116] J. Carron, A. Lewis, and A. Challinor, J. Cosmol. Astropart. Phys. 05 (2017) 035.
[117] P. Motloch and W. Hu, Phys. Rev. D **97**, 103536 (2018).
[118] X. Fang, T. Eifler, E. Schaan, H.-J. Huang, E. Krause, and S. Ferraro, Mon. Not. R. Astron. Soc. **509**, 5721 (2021).
[119] M. Raveri and C. Doux, Phys. Rev. D **104**, 043504 (2021).
[120] P. Lemos, M. Raveri, A. Campos, Y. Park, C. Chang, N. Weaverdyck, D. Huterer, A. R. Liddle, J. Blazek, R. Cawthon *et al.*, Mon. Not. R. Astron. Soc. **505**, 6179 (2021).
[121] G. Papamakarios, T. Pavlakou, and I. Murray, arXiv: 1705.07057.
[122] S. S. Boruah, T. Eifler, V. Miranda, and P. M. Sai Krishanth, Mon. Not. R. Astron. Soc. **518**, 4818 (2022).
[123] E. V. Linder, Phys. Rev. D **72**, 043529 (2005).
[124] S. Basilakos and F. K. Anagnostopoulos, Eur. Phys. J. C **80**, 212 (2020).
[125] D. Scolnic, D. Brout, A. Carr, A. G. Riess, T. M. Davis, A. Dwomoh, D. O. Jones, N. Ali, P. Charvu, R. Chen *et al.*, Astrophys. J. **938**, 113 (2022).
[126] N. Kokron, J. DeRose, S.-F. Chen, M. White, and R. H. Wechsler, Mon. Not. R. Astron. Soc. **505**, 1422 (2021).
[127] Z. Zheng, A. A. Berlind, D. H. Weinberg, A. J. Benson, C. M. Baugh, S. Cole, R. Davé, C. S. Frenk, N. Katz, and C. G. Lacey, Astrophys. J. **633**, 791 (2005).
[128] I. Zehavi, Z. Zheng, D. H. Weinberg, M. R. Blanton, N. A. Bahcall, A. A. Berlind, J. Brinkmann, J. A. Frieman, J. E. Gunn, R. H. Lupton *et al.*, Astrophys. J. **736**, 59 (2011).
[129] Ž. Ivezić, S. M. Kahn, J. A. Tyson, B. Abel, E. Acosta, R. Allsman, D. Alonso, Y. AlSayyad, S. F. Anderson, J. Andrew *et al.*, Astrophys. J. **873**, 111 (2019).
[130] O. Dore, C. Hirata, Y. Wang, D. Weinberg, T. Eifler, R. J. Foley, C. H. Heinrich, E. Krause, S. Perlmutter, A. Pisani *et al.*, Bull. Am. Astron. Soc. **51**, 341 (2019), https://ui.adsabs.harvard.edu/abs/2019BAAS...51c.341D/abstract.
[131] R. Laureijs, J. Amiaux, S. Arduini, J. L. Augueres, J. Brinchmann, R. Cole, M. Cropper, C. Dabin, L. Duvet, A. Ealet *et al.*, arXiv:1110.3193.
[132] M. Levi, L. E. Allen, A. Raichoor, C. Baltay, S. BenZvi, F. Beutler, A. Bolton, F. J. Castander, C.-H. Chuang, A. Cooper *et al.*, Bull. Am. Astron. Soc. **51**, 57 (2019), https://ui.adsabs.harvard.edu/abs/2019BAAS...51g..57L/abstract.
[133] P. Ade, J. Aguirre, Z. Ahmed, S. Aiola, A. Ali, D. Alonso, M. A. Alvarez, K. Arnold, P. Ashton, J. Austermann *et al.*, J. Cosmol. Astropart. Phys. 02 (2019) 056.
[134] K. N. Abazajian, P. Adshead, Z. Ahmed, S. W. Allen, D. Alonso, K. S. Arnold, C. Baccigalupi, J. G. Bartlett, N. Battaglia, B. A. Benson *et al.*, arXiv:1610.02743.